~~Onset of~~ Aegean-style extensional deformation in the contractional southern Dinarides~~ documented by incipient~~: Incipient normal fault scarps in Montenegro

Peter Biermanns[1], Benjamin Schmitz[2], Silke Mechernich[3], Christopher Weismüller[1], Kujtim Onuzi[4], Kamil Ustaszewski[4], Klaus Reicherter[1]

[1]Institute of Neotectonics and Natural Hazards, RWTH Aachen University, 52064 Aachen, Germany
[2]Institute of Geosciences, University Jena, 07749 Jena, Germany
[3]Institute of Geology and Mineralogy, University Cologne, 50937 Köln, Germany
[4]Institute of Geosciences, Energy, Water and Environment, Polytechnic University of Tirana, 1016 Tirana, Albania

Correspondence to: Peter Biermanns (p.biermanns@nug.rwth-aachen.de)

Abstract. We describe two previously unreported, 5-7 km long normal fault scarps (NFS) occurring atop fault-related anticlines in the coastal ranges of the Dinarides fold-and-thrust belt in southern Montenegro, a region under predominant contraction. Both NFS show well-exposed, 6-9 m high, striated and locally polished fault surfaces~~ in limestones,~~, cutting shallowly dipping limestone beds at high angles and documenting active faulting during the Holocene. Sharply delimited ribbons on free rock faces show different color, varying karstification and lichen growth and suggest stepwise footwall exhumation, typical of repeated normal faulting earthquake events. Displacements, surface rupture lengths and geometries of the outcropping fault planes imply paleoearthquakes with $M_w \approx 6 \pm 0.5$ and slip rates of ~~c.~~at least 0.3-0.5 mm/yr since the Last Glacial Maximum. ~~Slip~~Absolute (and more reliable, higher-resolution) slip rates based on cosmogenic ^{36}Cl data from the scarps are significantly higher: ~~modeling~~modelling suggests 1.5 ± 0.1 mm/yr and 6-15 cm slip every ~~c.~~ 35-100 yrs, commencing~~ c.~~, or resuming, ~6 kyr ago. The total throw on both NFS – although poorly constrained – is estimated to max. 200-400 m, and offsets the basal thrust of a regionally important tectonic unit. ~~Both~~The NFS are incipient extensional structures that postdate growth of the fault-related anticlines on top of which they occur. To explain their existence in a region apparently under purely contractional influence, we consider two explanation approaches possible: (i) syn-convergent NFS development or (ii) an hitherto unnoticed propagation of actual extensional tectonics from the hinterland. Interestingly, the position of the extensional features agrees with recent geodetic data, suggesting that our study area is located exactly at the transition from NE-SW-directed shortening in the northwest to NE-SW-directed extension to the southeast. While the contraction reflects ongoing Adria-Europe convergence taken up along the frontal portions of the Dinarides, the incipient extensional structures might be induced by rollback of the Hellenic slab in the SE, whose effects on the upper plate appear to be migrating along-strike the Hellenides towards the northwest. The newly found NFS possibly provide evidence for a kinematic change of a thrust belt segment over time. Alternatively, the NFS might be regarded as second-order features accommodating changes in dip of the underlying first-order thrust faults to which they are tied genetically.

1 Introduction

Active normal faults in the Mediterranean frequently develop bedrock normal fault scarps (NFS). Their suitability as tools for paleoseismic analyses has been proven by many authors (see following passages for differentiated references). We introduce~~e.g., Armijo et al., 1992; McCalpin, 1996; Benedetti et al., 2002; Papanikolaou et al., 2005, 2013; Grützner et al., 2013, 2016; Mason et al., 2016, 2017; Mechernich et al., 2018). We report~~ two previously unreported, 5-7 km long NFS along the southwestern slopes of the Rumija mountains in the coastal ranges of the Dinarides fold-and-thrust belt in southern Montenegro on the western Balkan Peninsula (Figs. 1 – 4; Figs. S1 & S2~~,~~; Table S3). According to their positions between the eponymous towns, we refer to them as *Bar* (BFS) and *Katërkolle* (KFS) *fault scarps*. The primary aim of this paper is a first-time description and interpretation of the mentioned structures, including (i) verification that BFS and KFS are active NFS at all, (ii) basic studies on the timing of NFS exhumation and slip rates, as well as (iii) a discussion on how these active NFS may be embedded in the contractional geodynamic setting of the southern External Dinarides. Our work is based on a thorough, multifaceted in-situ mapping campaign, followed by a low spatial resolution ^{36}Cl cosmogenic dating of NFS free-face samples. Both, paleoseismic interpretations based on overall NFS geometries and visual indicators (e.g., Armijo et al., 1992; McCalpin, 1996; Giraudi and Frezzotti, 1995; Roberts and Michetti, 2004; Papanikolaou et al., 2005, 2013; Papanikolaou and Roberts, 2007; Faure Walker et al., 2009; Grützner et al., 2013, 2016; Bubeck et al., 2015; Mason et al., 2016, 2017; Mechernich et al., 2018) as well as ^{36}Cl cosmogenic dating (e.g., Benedetti et al., 2002~~Both NFS~~, 2013; Palumbo et al., 2004; Schlagenhauf et al., 2010, 2011; Roberts et al., 2014; Tesson et al., 2016; Cowie et al., 2017; Mechernich et al., 2018; Goodall et al., 2021; Iezzi et al., 2021) have previously been successfully applied for NFS in the Mediterranean region, delivering valuable instructions and benchmarks for our study. BFS and KFS closely resemble the abundant and well-studied NFS in the Central Apennines (Italy; e.g., those ruptured during the 2016/2017 earthquake series) as well as ~~in~~ the Greek part of the Hellenides in terms of geomorphology, structural setup and length, showing evidence of segmentation and repeated co-seismic footwall exhumation during earthquakes (e.g., Papanikolaou et al., 2005, 2013, Grützner et al., 2016; Mason et al., 2016, 2017; Civico et al., 2018; Mechernich et al., 2018). ~~As the Italian and Greek examples suggest that~~While the formation of ~~such~~ large-scale NFS in the extensional geodynamic settings of Italy and Greece is ~~commonly correlated~~barely surprising, and the NFS correlate with strong extensional earthquakes, it is puzzling that all known major ~~historic~~instrumentally recorded earthquakes between ~~Southern~~southern Croatia and Albania (including e.g., *Montenegro 1979*, $M_w\approx7.1$, or *Durrës/Albania 2019*, $M_w\approx6.4$; e.g., Benetatos and Kiratzi, 2006; Papadopoulos et al., 2020) were exclusively contractional (Fig. 1). Two different explanations are discussed: (i) The ~~facts that (i)~~ NFS are formed syn-convergent, a phenomenon that has been frequently observed in other locations (e.g., Philip and Meghraoui, 1983; Nábělek, 1985; Avouac et al., 1992; Bennett et al., 2012, Hicks and Rietbrock, 2015; Corrado et al., 2019; Riesner et al., 2021), or (ii) the ~~occurrence~~NFS indicate a possible temporal transition in the kinematic behaviour of ~~these~~a mountain range – a phenomenon rarely documented in detail. The hitherto inchoate understanding of the newly discovered ~~extensional structures is still fully unexplained, (ii)~~Montenegrin NFS and the facts that (i) similar NFS in Italy and Greece are associated with major earthquakes ~~causing~~that caused many casualties and severe economic losses from destroyed medieval villages and modern infrastructure (e.g., Chiaraluce et al., 2017, Table S4) and ~~that (iii) smaller~~(ii) comparably small fault systems are generally underestimated in terms of their seismic hazard (Grützner et al., 2013), underline the urgent need to further analyse such structures. ~~Apart from~~In the ~~seismic hazard perspective,~~following, we present the ~~occurrence~~methods and results of ~~(possibly seismogenic)~~ NFS ~~in a purely contractional segment~~mapping (structural and surface exposure indicators), cosmogenic ^{36}Cl sample collection, preparation and AMS dating, modelling of ~~a fold-and-thrust belt indicates a possible temporal transition in~~ the ~~kinematic behaviour of a mountain range – a phenomenon rarely documented in detail and calling for a geodynamic explanation~~^{36}Cl data, and the resulting tectonic interpretations.

2 Geological setting

The BFS and KFS are located in the extreme south of the Dinarides, slightly north of the Dinarides-Hellenides transition. The latter is marked by the ca. NE-SW-striking normal-transverse Shkodra-Peja fault zone (SPFZ, e.g., Handy et al., 2019, and references therein). Driver for the seismicity along the coast of Montenegro and Albania is the Adriatic microplate~~, whose northward motion is accompanied by a bidirectional subduction~~ that bidirectionally subducts below the Balkan and Apennine peninsulas, creating almost mirror-imaged tectonic settings on both sides of the Adriatic Sea (e.g., Nocquet and Calais, 2004; Battaglia et al., 2004; Faccenna et al., 2014; Le Breton et al., 2017; Király et al., 2018). Both, the ~~Apennines and~~ Dinarides-Hellenides and Apennine fold-and-thrust belts are characterized by orogen-parallel, NW-SE-striking tectonic units. NE-SW-directed contraction along the deformation ~~front~~fronts is replaced by extensional domains in the hinterland (Fig. ~~1). The latter is~~1; e.g., D'Agostino et al., 2008; Nocquet, 2012) that are attributed to subduction-rollback, gradually migrating towards Adria in both cases (e.g., Cavinato and de Celles, 1999; Dumurdzanov et al., 2005; Carminati and Doglioni, 2012~~,~~; Handy et al., 2019). Despite all similarities between Dinarides-Hellenides and Apennines, seismotectonic characteristics ~~for the concerned areas~~ reveal major differences~~:~~. In Italy, the most destructive earthquakes are ~~dominantly within the~~ commonly normal faulting events, creating distinct large-scale NFS in a pronounced, continuous hinterland extensional domain~~, whereas in~~ (e.g., Galadini and Galli, 2000). On the Balkan peninsula, the ~~Dinarides-Hellenides, they are rather~~greatest risk emanates from contractional~~,~~ earthquakes with epicentres close to the Montenegrin/Albanian coast (e.g., Pondrelli et al., 2006; Copley et al., 2009; Chiaraluce et al., 2017; Papadopoulos et al., 2020; Vittori et al., 2020; Fig. 1). ~~Accordingly, large-scale normal faults are abundant in the~~ Known extensional ~~Apennines hinterland~~tectonics and related earthquakes are restricted to the internal Hellenides south of SPFZ, resulting from a clockwise rotation of the Hellenides segment with respect to the Dinarides (e.g., ~~Galadini and Galli, 2000), while they~~ Jouanne et al., 2012; Facenna et al., 2014; Handy et al., 2015). NFS are ~~less prominent in~~poorly developed in these regions of Albania (Handy et al., 2019) ~~and so far~~while they were hitherto entirely unknown in Montenegro. ~~We consider this view obsolete: the two newly reported NFS of Bar and Katërkolle (~~The discovery of BFS and KFS~~;~~ (Figs. 2 – 4; Figs. S1 & S2; Table S3) is therefore striking in two respects: (i) They are a rare example of well-developed NFS in the Dinarides-Hellenides north of Greece. (ii) They are surprisingly not located in the hinterland ~~away from the coast~~, where extensional focal mechanisms are well documented, but as close as 4 km from the coast, in a fold-and-thrust belt segment solely characterized by horizontal contraction, evidenced both in the geological structures and in the predominance of reverse faulting focal mechanisms (Fig. 1). Structurally, the BFS and KFS are located incutting the ~30° uniformly NE-dipping limestone beds of the Budva-Cukali Unit, at high angles. The Budva-Cukali Unit is a regionally important tectonic nappe in the Dinarides-Hellenides consisting mainly of Mesozoic pelagic sediments topped by Paleogene synorogenic deposits (Fig. 4). In the study area, along the Rumija mountain front, only the uppermost part of its stratigraphic section appears as a c. ~50 m wide corridor between the structurally underlying Kruja-Dalmatian and the overlying High Karst tectonic units. Furthermore, the Budva-Cukali Unit appears in remnants at the base of the High-Karst Unit in two isolated nappe outliers (Fig. 4). For more detailed information on the regional geology of the area, the reader is referred to, e.g., Biermanns et al., 2019; Schmid et al., 2020; and Schmitz et al., 2020. Current horizontal shortening rates for thisthe region lie in the range of 3-5 mm/yr (Kotzev et al., 2008; Jouanne et al., 2012; Devoti et al., 2017), while vertical uplift rates were estimated to around 1 mm/yr (Biermanns et al., 2019 *and references therein*).

3 Methods

3.1 Fieldwork

3.1.1 Structural and morphological mapping, site selection and fault scarp profiling

The full extent of BFS and KFS was geologically and structurally mapped to gain details of fault morphology and orientation, fault striae, surface roughness and lichen growth (Fig. 4; Figs. S5 – S8). Based on the mapped fault lengths (Table S9) and an evaluation of Particular attention was directed to the identification and mapping of striation-perpendicular, ca. slope parallel horizons on the fault planes, interpreted to display coseismic displacements per earthquake event (Figs. 3 B and S6,; more detailly described in sectionSection 4.1),) Based on the mapped fault lengths (Table S9) and an evaluation of the mentioned horizons, we calculatedestimated earthquake magnitudes after Wells and Coppersmith (1994). Furthermore, four representative sites (BFS_N, BFS_{S1}, BFS_{S2} and KFS; Figs. 4 & S1; Table S3) were selected to collect samples for ^{36}Cl dating (site BFS_N only; see following Section 3.1.2) and to estimate low-resolution long-term (post-Last Glacial Maximum, LGM) slip rates based on topographic profiles across the fault scarps for comparison (Fig. 5, following examples of e.g., Papanikolaou et al., 2005; Mason et al., 2016) and to collect samples for ^{36}Cl dating (see Section 3.2). The four sites fulfil all essential requirements like minimum erosion and deposition, flat scarp base, intact scarp surface and representative striations (e.g., Bubeck et al., 2015; Cowie et al., 2017; Mechernich et al., 2018). The fault planes were cleared from vegetation (particularly for ^{36}Cl dating, Fig. 6),, followed by a thorough structural survey including the immediate surroundings. Profiles were measured by broomstick and clinometer parallel to striations in 1-m steps, c. ~50 m upslope and downslope the NFS. The entire NFS height consists of two sections: (i) height of the distinct free-face and (ii) degraded NFS height, interpolated from hanging wall and footwall slope (Fig. 5). Based on these, we calculated two sets of generalized post-LGM (18 ± 3 kyr) movement, e.g., Papanikolaou et al., 2005; for discussion see Section 5.3) slip rates for each site: (i) A conservative one, only considering slip on the visible free-face and (ii) a progressive one, incorporating the degraded NFS in prolongation of the free-face (Table S10). Since the calculation principle integrates the NFS heights over a full post-LGM time period, the method only yields hypothetical constant slip rates but does not resolve e.g. slip clustering or disclose possible phases of fault activity or quiescence. Despite these weaknesses and the availability of an absolute ^{36}Cl dating for site BFS_N (see Section 3.1.2), we still consider the comparison of topography-based slip rate estimations a reasoned benchmark in the frame of our study: (i) The mentioned four sites are distributed across different sections of BFS and KFS (Fig. 4) of which each has a distinct setup (e.g., structurally and in terms of exposition). (ii) The qualitative calculation normalised to a full post-LGM time frame sets an absolute lower limit in terms of slip rates and earthquake recurrence intervals.

3.1.2 ^{36}Cl dating: sampling procedure

Samples for ^{36}Cl dating were taken at site BFS_N (introduced in Section 3.1.1; Figs. 3 E ~~&~~, 6 & S2; Table ~~S2~~S3). For extraction of datable rock samples, a trace across the highest part of the outcrop wall was defined parallel to the visible striations (Fig. 6 C & F; q.v. Mechernich et al., 2018). To achieve an adequate resolution for the reconstruction of long-term slip rates and seismic events, we chose a sample spacing of ~~ca.~~ ~50 cm parallel to slip direction whilst avoiding confounding factors (e.g., joints, Fig. 6~~-~~ F). This sample spacing is rather large compared to previous studies of cosmogenic fault scarp dating and hence it is not possible to identify the stepwise ^{36}Cl concentration pattern (so-called cusps, e.g. Schlagenhauf et al., 2010). In our study, this is not a disadvantage, since the capable offsets of the small faults are lower than the ~2 m coseismic offset required for the generation of a stepwise ^{36}Cl concentration pattern. We take the low sample density into account in the modelling approach. As published, such resulting modelled slip rates are comparable to slip rates derived from dense (continuous) sampling (Beck et al. 2018; Iezzi et al., 2021). Generally, the multiparametric approach of our study compensates the low sample amount, as conclusions and interpretations are not solely contingent upon ^{36}Cl dating-based input data. The lowermost samples were collected ~~ca.~~ ~1 m below the scarp base by manual excavation of a trench (Fig. 6~~-~~ C). These buried samples are essential to characterize pre-exposure conditions (e.g., ~~Mechernich~~Cowie et al., ~~2018~~2017). The previously marked 15 x 5 cm sample blocks were carefully extracted with the help of an angle grinder, hammer and chisel (Fig. 6 D~~-~~ – F). Subsequently they were marked according to their distance from the scarp base and packed for shipping. To quantify the risk of insolation weathering at the sampling sites, exposure angles were determined in 10° steps with the help of a clinometer.

3.2 ^{36}Cl dating: sample preparation and data modelling

3.2.1 Sample preparation

Based on a spacing of 100-200 cm (striation-parallel distance on the fault plane), six sample blocks from sampling site BFS_N were prepared at the Institute of Geology and Mineralogy of the University of Cologne. Weathered parts and pore surroundings were carefully removed with a rotary tool before crushing and sieving. The following chemical treatment and the measurement at the CologneAMS facility were performed as described in Mechernich et al. (2018). Resulting ^{36}Cl/^{35}Cl, ^{36}Cl/^{37}Cl, and

$^{35}Cl/^{37}Cl$ ratios were used to calculate the concentrations of ^{36}Cl and natural chlorine (Cl_{nat}). Their reliability is confirmed by the simultaneous preparation of CoCal-N ^{36}Cl standard material (Mechernich et al., 2019) and one blank in the respective batch. The blank subtractions were 0.8–1.7 % (~~Tab.~~Table S11). The calculated ^{36}Cl concentrations of the 6 analysed samples range from ~7 × 10^4 at/g rock at 0.55 m below the scarp base to ~2 × 10^5 at/g rock at a height of 5.8 m above the scarp base. In general, the concentrations are continuously increasing with fault scarp height (Fig. 7). The ~~natural chlorine~~Cl_{nat} concentrations are very low, from 6 to 17 µg/g (~~Tab.~~Table S11). One replicate sample was prepared and measured in Cologne (~~Tab.~~Table S11). An aliquot of each dissolved sample was analysed by in-house ICP-OES at the University of Cologne to determine the concentrations of the principal ^{36}Cl target elements, Ca, K, Ti, and Fe. The ICP-OES Ca concentrations of the BFS_N-samples range from 38.9% to 40.0%, indicating local variabilities (~~Tab.~~Table S13) with a minor impact on the ^{36}Cl production rate. We used one ~~none~~non-treated free-face sample from the BFS_N site as a reference for the assumed thermal and epithermal neutron flux and thus constrain production of ^{36}Cl on ^{35}Cl. Equally, trace element analyses on ~~these~~this sample were used for the ^{36}Cl production estimate (~~Tab.~~Table S13). Both analyses were performed by Actlabs (Canada). For the hanging wall composition, we used the soil composition of the colluvium.

3.2.2 ^{36}Cl scarp modelling method and parameters

To determine earthquake ages from the ^{36}Cl concentrations, we used the Matlab® code of Schlagenhauf et al. (2010) that models synthetic ^{36}Cl concentrations while accounting for all influencing factors, i.e., the time-dependent variability of the fault scarp geometry, the chemical composition and the respective amount and timing of progressive exhumation. The code was adapted to the large sampling spacing and the mapped ribbon heights were added to the input parameters. All input parameters are described in the following ~~section~~passages and in Tables S11 – S13. Several parameters have an influence on the production of cosmogenic ^{36}Cl, which typically extends ~~to~~from several meters to tens of meters below the surface. In addition to the chemical composition and density of the bedrock scarp and the colluvial wedge (~~Tab.~~Table S12), the ^{36}Cl production rate depends strongly upon the rate at which the scarp is exhumed. Continuous accumulation of ^{36}Cl in the footwall rock occurs both in the shallow sub-surface (inherited or pre-exposure component) and to the largest part ~~as the scarp becomes~~after sub-~~aerially exposed~~aerial exposure and ~~grows higher~~growth of the fault scarp (e.g., Schlagenhauf et al., 2010; Mechernich et al., 2018). This typically leads to increasing ^{36}Cl concentrations with fault scarp height, although this is somewhat complicated by erosion of the scarp free-face, whereby ^{36}Cl in the rock is reduced by weathering. Furthermore, production rates have to be scaled appropriately to the local and distant shielding of the site from cosmic rays and ~~for~~to changes of production through time due to geomagnetic field effects. ~~In general, large offsets result in a stepwise pattern of ^{36}Cl concentrations (e.g., Schlagenhauf et al., 2010). For the latitude and height of our study side, an offset of at least ~2 m is required. Hence, the coseismic offsets of ~5-15 cm as observed from the ribbon mapping (see section 4.1) are significantly too low to generate such stepwise ^{36}Cl pattern.~~ The average density of the limestone samples was determined using the sample weight and their volume by suppression in water yielding 2.55 g/cm^3. The density of the colluvium was estimated at ~1.5 g/cm^3; more specific measurements were not undertaken due to local variabilities in the clast occurrence and humidity impact. We used a ^{36}Cl production rate of 48.8 ± 3.4 at/g/yr from Ca-spallation (Stone et al., 1996) as it is derived from a similar latitude (39°N), a rather comparable altitude (1445 m a.s.l.) and integrates over a time-span of 17.3 kyr, which is appropriate for our postglacial focus. All further production rates used are given in Table S13. Scaling with respect to latitude and elevation was performed using the Stone (2000) scaling scheme assuming a constant geomagnetic field intensity. The geometry of the fault as derived from the topographic profile (Fig. 5) is used to calculate shielding factors for the time-dependent self-shielding during the progressive exhumation of the fault plane. Thereby, 33° was used for the dip of the hanging wall, 56° as dip of the fault plane, 35° as dip of the footwall and 22.2 m as the total displacement of the hillslope. An additional topographic shielding does not occur since the mountains in sight occur just insignificantly above the horizon. There is a significant local variation in the amount of weathering of the exposed fault plane, ranging from zero at locations ~~of~~with preserved slickensides (0-3 m of the free-face height) to ~3 cm at the solution flutes. While the fault plane at the scarp base is smooth at a mm-scale, rock surface relief at 8.0-8.8 m height is 2-8 mm around the sampling line. Assuming this as the minimum amount of erosion and using a preliminary calculated ^{36}Cl age of ~15 kyr at 8.8 m height, we estimate an erosion rate of ~1 mm/kyr at our sample locations. Such a low rate was also observed on other fault planes in carbonates (Goldberg et al., 2016; Mechernich et al., 2018). The parameters used in the numerical modelling of the ^{36}Cl concentration with the Matlab® code *modelscarp.m* presented in Schlagenhauf et al. (2010) are displayed in ~~Tab. S14.~~Table S14. The code was used by iteratively modelling constant slip rates of the Bar fault, which fit the measured ^{36}Cl concentrations best. The modelling of "constant" arbitrary slip rates is done by using simple scenarios of a stick-slip behaviour with 6-15 cm coseismic offsets (as suggested by the mapped ribbons; approach is described in detail in the Supplementary information of Mechernich et al., 2018). The uncertainty of the constant slip rate is mainly based on the coverage of the measured ^{36}Cl concentrations and some minor points like the amount of coseismic offset, and additionally on external effects which are not incorporated in the given slip-rate uncertainty (e.g. deviations of production rate, shielding). We applied the criteria that all scenarios covering the 68% uncertainties of at least 3 of the 5 ^{36}Cl samples are considered, so that a 1σ in ^{36}Cl-internal uncertainty of this constant slip rate is derived. To approach the lowest possible slip rates on the Bar fault, we additionally applied a "sliding scenario" for the fault scarp part above the sampled part of the free-face, even though we did not find any indicators of such a "sliding event". Here as well we used the code *modelscarp.m* and iteratively tested which amount of sliding at which time results in the lowest slip rate for the sampled part of the free-face. The slide itself was modelled using a large offset within a small amount of time (i.e., 1 yr).

4 Results

4.1 Structure and morphology of the fault scarps

Both, the BFS and KFS crosscut the ~~c.~~ ~30° northeast-dipping beds of the Budva-Cukali tectonic zone at high angles (Figs. 5 & S5). Bedrock limestone in the footwall is juxtaposed against carbonatic, partly cemented colluvium and slope scree in the hanging wall, consisting of cm- to m-sized clasts (Figs. 3 B & C). The fault zone is marked by a cataclastic fault breccia of

≥ 1 m width (Fig. 3 D). Fault dip directions, pervasive slickenside striations, slickenfibres, Riedel shears, well-developed triangular facets and wine-glass-shaped valleys (Fig. 3 A & C; e.g., Dramis and Blumetti, 2005) prove active normal faulting. The total throw of the NFS is estimated to max. ~200 - 400 m~~,~~. The 200-m frame is based on the offset of stratigraphic markers across KFS (see cross sections ~~across KFS (~~in Fig. 4 C). The 400-m frame is based on an analysis of topographic cross sections across BFS, where a clearly perceptible knickpoint (~850 m a.s.l.) marks the NFS ~400 m below the overlying highest parts of the Rumija ridge (~ 1250 m a.s.l.). Free-faces are 1-9 m high in domains with negligible erosion (Figs. 3 E & S2 C), and up to 40 m in domains of strong hanging wall erosion, e.g., where gullies occur (Fig. 3 A & C). Fault planes frequently exhibit ~~c.~~ ~5–50 cm wide, horizontal and sharply bound ribbons of distinct colour and roughness, increasingly better preserved toward the scarp base (Figs. 3 B & S6). ~~Widths~~Boundaries between the ribbons are ca. perpendicular to local fault plane striations and therefore mostly slope-parallel. Their distance to the present-day scarp base is nearly – but not perfectly – constant. Across these boundaries, widths of karstic solution flutes, roughness, lichen growth and micro-karstification decrease stepwise toward the scarp base (Fig. S6). ~~These~~While the lower ribbons are partly correlatable over longer distances, the higher-up ones are often hardly distinguishable and defaced local occurrences. Individual ribbons can be correlated across several locations in terms of their width and habitus (Fig. S7). However, they are rather isolated occurrences that do not enable a gapless tracing along the fault planes. The highest density of perceptible single horizons was encountered on BFS$_{S}$. The ribbons are interpreted as single exhumation events (e.g., Mechernich et al., 2018 *and references therein*~~).~~; for further discussions see Section 5.1) and therefore used as an input parameter for 36Cl dating (see Sections 3.2.2 and 4.2.2). The BFS dissects the slopes of Mt. Lisinj (Fig. 2). Approximately midway along its ~~c.~~ ~5-km-extent, it ~~significant~~ changes its mean fault plane orientation from moderately steep (~55°) ~~c~~ca. NNW-SSE striking in the north, to steep (~70°) ~~c~~ca. east-west striking in the south (Figs. 4, S5 and S7 A & B). ~~Since no conclusive outcrops were found in the~~The transitional area~~, a connection of~~ between the northern (BFS$_{N}$) and southern (BFS$_{S}$) section of BFS ~~is not fully provable (Fig.~~presents itself rather complex, with an apparently diffuse array of multiple fault planes (Figs.4, S1 & S8~~,~~; Table S3). Despite fewer conclusive outcrops, the pervasiveness of faults in bare rock and relays at the transition between major branches of BFS$_{N}$ and BFS$_{S}$ (mapped by means of remote sensing) likely prove an interconnection of both BFS sections (Fig. S15). The formation of distinct NFS outcrops (like in most other locations) is likely prevented by lower offset as a result of slip distribution among multiple fault branches. Ribbon abundance and widths are comparable along the full length of BFS (Fig. S7 A & B). KFS follows the southern slopes of the Rumija mountains for >7 km and crosscuts thrusts at the base and top of the Budva-Cukali zone (Fig. 4). A connection between BFS$_{S}$ and KFS is conceivable, as suggested by (i) a similar mean fault plane orientation and (ii) an interjacent penetrative step in terrain steepness (Fig. S8). However, a lack of intermittent outcrops for ~~c.~~ ~3 km along-strike and less abundant ribbons (Fig. S7 C) render such correlation less certain. Along all NFS sections, fault planes reveal systematic undulations and corrugations with wavelengths up to several meters (Fig. 3 C). The trends of striations follow the mean fault plane orientation, indicating dominant dip-slip kinematics. A tendency to increasing strike-slip components away from the section centres creates patterns of radially outward-diverging striations (Fig. S5). At several locations along BFS$_{N}$ and KFS, transfer faults were mapped (Fig. 4 A). These faults branch away obliquely from the main fault plane, sometimes at high angles. The free faces formed by these faults are commonly less high (~1 - 4 m) as compared with the main NFS, but otherwise show the same characteristics (slickenside striations, undulations etc.). The western end of KFS is marked by a large-scale (10s of meters high; cleared by an adjacent stream) fault plane that deviates northward from the main KFS trend by almost 90° (Fig. 4 A) and features slickensides indicative of strike-slip movement.

4.2 Proxies for fault scarp exhumation

4.2.1 Slip rate and magnitude estimates derived from fault scarp profiling, surface rupture lengths and ribbons

SetsFor all four NFS sampling sites (i.e., also those that were not dated by means of the ^{36}Cl method), sets of conservative and progressive minimum slip rates were calculated according to the simplistic procedures described in Section 3.1.1. The obtained conservative rates range between 0.34 ± 0.07 (site BFS$_{S2}$) and 0.49 ± 0.10 (site BFS$_N$) mm/yr. The progressive rates vary between 0.41 ± 0.08 (site BFS$_{S2}$) and 1.23 ± 0.25 (site BFS$_N$) mm/yr (Table S10). Measurements of earthquake-related ribbons (see also Section 4.1) in a total of 48 sites (Fig. S11S7) revealed up to five horizons per location, with 15 cm average and 5-50 cm individual ribbon width. While the lower ribbons are partly correlatable over longer distances, the higher-up ones are often hardly distinguishable local occurrences. The highest density of single horizons was encountered on BFS$_S$. An average displacement of 15 cm/event on a representative free-face (e.g., at site BFS$_{S1}$, ≈6.5 m high) yields an approximate average recurrence interval of ~400 yrs. MagnitudeThe lower three horizons at site BFS$_N$ (from bottom to top: 15 ± 1 cm; 11 ± 1 cm; 5.5 ± 1 cm) were used as input parameters for (the more reliable) ^{36}Cl dating-derived earthquake ages with significantly different results (see following Section 4.2.2). Rough magnitude calculations after Wells and Coppersmith (1994) arewere based on the input parameters (ribbon widths and fault lengths) presented in Table S9. As particularly the connection between different NFS sections and NFS genesis are not trivial, we use different presumptions and calculation methods. Derived magnitudes range from M$_w$≈5.3 to 6.5.

4.2.2 Slip rates and earthquake ages obtained from ^{36}Cl dating

Slip rates derived from modelling the ^{36}Cl concentrations on the BFS$_N$ free-face indicate exceptionally high slip rates of 1.5 ± 0.1 mm/yr for the simplest scenario of a stick-slip behaviour (ca. 6-15 cm slip every ca. 35-100 kyr, Fig. 7) in which the 8.8 m-high free-face was exhumed within the last 5.9 ± 0.4 kyr (Fig. 7 B), without 10% production rate uncertainty. The according fault scarp age is presumably 14.8 +- 1.0 kyr (Figure 7 B). Earthquake ages of 100 ± 14 yrs (EQ1), 173 ± 24 yrs (EQ2) and 210 ± 29 yrs (EQ3) (Fig. 8) were estimated using the mapped coseismic slips of 15 ± 1 cm (EQ1), 11 ± 1 cm (EQ2) and 5.5 ± 1 cm (EQ3). Hence, the earthquake-recurrence interval is around 35-100 years. Alternative interpretations of the ^{36}Cl data (see Section 5.2) are conceivable but significantly more complicated and hence considered less likely.

The modelling of the ^{36}Cl concentrations on the BFS$_N$ free-face highlights that the measured ^{36}Cl pattern can be generated by a constant slip rate of 1.5 ± 0.1 mm/yr (Fig. 7 A). Since all five samples are aligned pretty well to fit this synthetical slip rate of ~1.5 mm/yr, we feel that it is robust. Tests of using different amounts of coseismic offsets did not reveal significant deviations. The given uncertainty does not include external factors like the ~10% production rate uncertainty which affects all ^{36}Cl samples in the same way. However, it covers the 68% confidence interval for at least 3 of the 5 ^{36}Cl samples (Fig. 7 A) and can hence be considered as 1σ internal reliability. Based on this uncertainty we did the further calculations of free-face and fault scarp ages as well as earthquake ages. The retrieved slip rate suggests that the 8.8 m-high free-face was most likely exhumed within the last 5.9 ± 0.4 kyr (Fig. 7 B) and the according fault scarp age is presumably 14.8 ± 1.0 kyr (Fig. 7 B). The earthquake ages were estimated by injecting the mapped coseismic slips of the ribbons around site BFS_N (15 ± 1 cm for EQ1, 11 ± 1 cm for EQ2 and 5.5 ± 1 cm for EQ3) in the ^{36}Cl-model (this method is described in detail in Mechernich et al., 2018). The resulting earthquake ages are 100 ± 14 yr (EQ1), 173 ± 24 yr (EQ2) and 210 ± 29 yr (EQ3; Fig. 8). These ages also consider the uncertatinties of the ^{36}Cl production rates. Hence, the earthquake recurrence interval appears to be around 35-100 yrs. Since the slip rate of 1.5 ± 0.1 mm/yr is very high, we tested how to receive the lowest possible slip rate explaining the ^{36}Cl data. To be as open-minded as possible, we used any hypothetical scenario, without correlation to the local mapping. The lowest slip rate on the samples free-face is achieved when minimizing its inherited component of ^{36}Cl which is generated in the subsurface. The minimum amount in inheritance is caused by a very fast exhumation of the upper scarp, e.g. by a sliding event, which exhumes 14.5 m in a very fast time (1 yr in the modelling code; Fig. 7 C & D). Before this hypothetical sliding event, the hillslope was exposed for an arbitrary 200 yrs (from 6.7 ± 0.6 kyr to 6.5 ± 0.6 kyr; Fig. 7 D). After the hypothetical sliding event, the stick-slip modelling as described above revealed the best fitting for a slip rate of 1.15 ± 0.10 mm/yr during the last 6.5 ± 0.6 kyr (Fig. 7 C). Hence, we highlight that the slip rate of the Bar fault during the last ~6 kyr was surely higher than ~1.15 mm/yr and presumably around 1.5 ± 0.1 mm/yr. Also, alternative interpretations of the few ^{36}Cl data points is conceivable, but they are significantly more complicated, not underlined by field findings and hence considered less likely. The reliability and uncertainties are evaluated in the discussion Section 5.2.

5 Discussion

5.1 ~~Reliability~~Interpretation of ~~slip rates from~~ ribbons, surface rupture lengths and magnitude estimation

The described ribbons on fault planes (see Section 4.1) are often correlatable across several locations based on their habitus and constant widths, while commonly showing sharp boundaries (Figs. 3 B, S6 & S7 A-C). We interpret these characteristics to exclude any kind of gradual or localized exhumation by erosion or gravitational processes (see also Section 5.4). For example, erosion from human or animal activity (despite being very unlikely in such remote, steep and overgrown terrain) would neither yield such constant ribbon widths over long distances, nor would it account for repeated, cm-scale exhumation in relatively large time steps (as suggested by the different states of surficial weathering, see Section 4.1). Weather/climate- (i.e., precipitation-) related exhumation would show more gradual transitions between individual ribbons and/or create inconstant ribbon widths due to (topography-related) non-uniform surface runoff. Snow – as the only conceivable weather-related factor – is ruled out, since it is an extremely short-lived phenomenon in this coastal climatic setting at low elevation. Aside from the local snow's non-existent capability of leaving distinctly visible marks, it would possibly never create such uniform ribbon widths, as snowdrifts would certainly yield variable thicknesses of the snow blanket. Gravitational sliding of material at the scarp base may occasionally occur. However, we regard this as a phenomenon restricted to particularly susceptible ('exposed', steep) locations along the fault scarp. Therefore, such processes would equally not create uniform ribbon widths over long distances, but rather deface existing ones. Based on this argumentation, the attribution of the observed ribbons to individual seismic events is highly ascertained. This technically qualifies the ribbons as input parameters for magnitude calculations after Wells and Coppersmith (1994). Minor error sources are misinterpretations of displacement per event, as ribbons may be defaced and overseen. When using fault lengths as input data for the Wells and Coppersmith (1994) method, incorrect recognition of the actual fault lengths constitutes a similar minor error source (see also Section 4.2.1; Table S9). The most severe error source, however, is the application of the empirical approach itself. For our setting with short fault lengths and relatively low magnitudes (i.e., $M_w<6$), Wells and Coppersmith (1994) only present limited data so that the adequacy of this statistical method is questionable. Depending on the interpretation of our NFS in a per-se contractional setting (see Section 5.4), they may portray magnitudes ranging ~1 M below the actual magnitude evoked by the rupture of first order thrust faults – a phenomenon that can, e.g., be observed on Crete, where $M_w \approx 8$ (or higher) uplifted the western part, whereas onshore normal faults are much shorter but also seismogenic with $M_w \approx 6 \pm 0.5$.(e.g., Grützner et al., 2016; Mason et al., 2016; Schneiderwind et al., 2017). The obtained values would therefore advance to magnitudes in the range of the Montenegro 1979 earthquake, which are likelier to produce crustal ruptures of such scale (e.g., McCalpin, 1996).**profiling**

For our classical derivation of slip rates, we assumed that preservation of NFS initiated around the LGM, c. 18 ± 3 kyr ago, in the Mediterranean region (e.g., Benedetti et al., 2002; Papanikolaou et al., 2005; Giraudi & Frezzotti,1995). Until then, periglacial conditions allowed slope degrading processes to exceed fault throw rates. Post-LGM warming, waning freeze-thaw cycles and slope stabilization by vegetation allowed fault throw to outpace slope degradation, thus forming pronounced NFS (e.g., Papanikolaou et al., 2005). Estimating slip rates using free-face heights holds two main error sources: (i) The exact timing of LGM and NFS formation onset and (ii) the interpretation of NFS geometry. For our study, (i) is well-constrained by similar studies from Greece and Italy (e.g., Giraudi & Frezzotti, 1995; Kuhlemann et al., 2009; Papanikolaou et al., 2013). According to Papanikolaou et al. (2005) *and references therein*, the initiation of NFS formation is shifted to ages <18 ka. This and the fact that parts of the free-faces have been eroded between ~18 ka and today, make our estimates a conservative minimum. The estimation of errors connected to (ii) is more complex and related to both tectonic and erosional impacts. Unknown proportions of the presently degraded fault scarps were formed both pre/syn- and post- LGM. The effect of ongoing (but reduced) erosion after formation of the NFS highly varies for different segments. The KFS and BFS_S are south- (i.e., not sea-) facing and better protected by vegetation. Especially for BFS_S, dissection by erosional gullies is minimal. Free-faces are steep and moderately high, degraded scarps less developed and earthquake ribbons well-visible and abundant (Fig. S7 B). By contrast, BFS_N is more exposed to weathering (i.e., sea-facing, surrounded by less vegetation) and dissected by numerous gullies (Figs. 3 & S1). Here, more degraded scarps, high, shallowly dipping free-faces and fewer earthquake ribbons are observed (Fig S7 A). We hence consider profiling sites BFS_{S1} and BFS_{S2} to provide the most reliable results. Assuming low amounts of local post-LGM erosion at the selected sites, we favour purely free-face-based rates. A comparison with calculations including the degraded NFS (Table S10) shows that our conservative rates are, if at all, probably only exceeded by minimal amounts.

5.2. Reliability of slip rates and ages from ^{36}Cl dating (site BFS_N)

The applied forward modelling method accounts only for the analytical ^{36}Cl uncertainties and not for the uncertainties of the parameters introduced in Section 3.2.2 and Table S13. Changes of these input parameters would shift the modelled earthquake ages to older or younger values, without changing the relative recurrence interval (e.g., Mechernich et al., 2018). The largest effect of such a parameter change is related to the ^{36}Cl production rates from Ca-spallation or muon capture. A change of these two rates in the frame of published uncertainties would systematically shift all ages and slip rates within ~10%. This shift is included in the age calculations but not in the slip rate calculations. Furthermore, the estimated parameters for the density of the colluvium, the erosion rate, and the apparent pre-exposure duration can cause similar shifts of the calculated ages. Changes in the erosion rate, e.g., using the minimum erosion rate of 0 mm/kyr would result in 3% younger ages at the top of the free-face compared to the used 1 mm/kyr which was chosen based on the 2-8 mm of relief at the top of the free-face. Due to the large degraded part of the fault scarp, the choice of the apparent pre-exposure duration has no impact on the restored slip history of the free-face. In Section 4.2.2According to the mapping results of the ribbons, we suppose a stick-slip behaviour of the NFS as the most likely scenario for the interpretation of ourthe ^{36}Cl data. The few data points itself would indeed leave a margin for other scenarios, e.g., a landslide/rockfall that exhumed the degraded part of the scarp ~6.5 kyr ago, followed by free-face exhumation (Fig. 7 C & D). However, this is ruled out by the fact that no indicators of landsliding were found in the hanging wall at all. Furthermore, the modelled slip rate for this scenario would be as well very high (~1.1-1.2 mm/yr), owing to the clearly increasing ^{36}Cl concentrations with scarp height. Several more complicated scenarios are possible but they would require a larger amount of samples and could be to topic of future studies. This study aimed to estimate the slip rate of the free-face, which is likely to be 1.5 ± 0.1 mm/yr, owing to the clearly increasing ^{36}Cl concentrations with scarp height and the mapping of the ribbons and surrounding geology. Also the very young past earthquake ages of 100 ± 14 yr (EQ1), 173 ± 24 yr (EQ2) and 210 ± 29 yr (EQ3) are quite robust according to the combination of ^{36}Cl data with the mapping of exposure duration. Concerning the upper part of the fault scarp, we have a lack of data for clear. An extrapolation of the ~1.5 mm/yr of slip on the free-face would result in a fault scarp age of 14.8 ± 1.0 kyr. This is a reasonable age also found for several fault scarps in the high altitude of the Apennines (e.g. Cowie et al., 2017; Beck et al., 2018). The estimated ~200-400 m offset presented in Section 4.1 indicate incipient activity of the Bar normal fault. Extrapolation of the calculated slip rate of ~1.5 mm/yr and using the maximum offset of 400 m results in a potential initiation time ~270 kyr ago.

5.3. ~~Interpretation~~ Reliability of ~~ribbons, surface rupture lengths~~slip rates obtained from fault scarp profiling

As described in previous chapters, ^{36}Cl dating was conducted for one site (BFS_N) only. To enable a comparison of the different (structurally and exposure-related distinct) sections of the fault scarps nonetheless – and to provide at least one benchmark for the obtained ^{36}Cl dating results – we invoke the rather simplistic technique of fault scarp profiling (see also Sections 3.1.1 and 4.2.1) for slip rate derivation. For this technique, it is assumed that the preservation of NFS initiated around the LGM in the Mediterranean region (e.g., Benedetti et al., 2002; Papanikolaou et al., 2005; Giraudi & Frezzotti,1995). Until then, periglacial conditions allowed slope degrading processes to exceed fault throw rates. Post-LGM warming, waning freeze-thaw cycles and slope stabilization by vegetation allowed fault throw to outpace slope degradation, thus forming pronounced NFS (e.g., Papanikolaou et al., 2005). The applied slip rate estimation using free-face/NFS heights holds three main error sources: (i) The local impact of LGM climate on erosion at all, (ii) the exact timing of initiating fault scarp preservation – in case it was effectively impeded during glaciation – and (iii) the interpretation of NFS geometry. Being aware that the exact timing of the (local) LGM is a matter of debate, we synthesized 18 ± 3 kyr as an adequate time frame for our location (based on available data and literature from surrounding areas in the Balkans, Greece and Italy; e.g., Giraudi, 1995; Giraudi and Frezzotti, 1995, 1997; Allen et al., 1999; Kuhlemann et al., 2009; Papanikolaou et al., 2005, 2013). However, the large variety of ages presented in literature (for comparison, e.g., Pope et al., 2017; Pavlopoulos et al., 2018) still cause us to admit a rather large degree of uncertainty concerning this value. The estimation of errors connected to (i) and (iii) is no less complex and related to both tectonic and climatic/erosional impacts. Even if the above specified LGM-timing is accurate for a broader region, small-scale local variations may exist, e.g., as a result of a location's elevation, exposition and microclimate. When interpreting the NFS geometries, it has to be kept in mind that unknown proportions of the presently degraded fault scarps were formed both pre/syn- and post- LGM. The effect of ongoing (but reduced) erosion after the LGM may highly vary for different segments. The KFS and BFS_S are south- (i.e., not sea-) facing and better protected by vegetation. Especially for BFS_S, dissection by erosional gullies is minimal. Free-faces are steep and moderately high, degraded scarps less developed and earthquake ribbons well-visible and abundant (Fig. S7 B). By contrast, BFS_N is more exposed to weathering (i.e., sea-facing, surrounded by less vegetation) and dissected by numerous gullies (Figs. 3 & S1). Here, more degraded scarps, high, shallowly dipping free-faces and fewer earthquake ribbons are observed (Fig S7 A). We hence consider profiling sites BFS_{S1} and BFS_{S2} to provide the most reliable results when using this particular method. Assuming low amounts of local post-LGM erosion at all selected sites, we favour purely free-face-based rates. A comparison with calculations including the degraded NFS (Table S10) shows that our conservative rates are, if at all, probably only exceeded by minimal amounts.~~**magnitude estimation**~~ Provided that the introduced quantitative NFS profiling method is rather error-prone (see discussion above) and low-resolution, we again stress that it was used as an auxiliary tool complementing the ^{36}Cl dating method (see Sections 3.1.2, 3.2.1, 3.2.2, 4.2.2 and 5.2). The obtained ^{36}Cl ages confirm the assumed post-LGM formation of BFS and KFS but suggest an initial exhumation of the present BFS_N free face only ~6 kyr ago. We stress that the obtained ~6 ka likely mark the first post-LGM fault movement, initiating the development of a pronounced surficial expression toward the present NFS. However, we do not generally exclude pre-

LGM activity on the faults, followed by a long period of quiescence (i.e., slip clustering). A predecessor (pre-LGM) fault scarp may have existed before falling victim to erosion. Due to the fact that ribbon widths, general NFS heights and morphologies as well as profiling-derived slip rates (Section 4.2.1; Table S10) are similar across BFS_N, BFS_S and KFS – and considering that all segments are in close proximity to each other – we expect the ^{36}Cl-derived exhumation history and slip rates of BFS_N to be valid for the full extent of BFS and KFS.

The attribution of earthquake ribbons to individual events is highly ascertained as they are often correlatable across several locations and many of them show sharp boundaries (Figs. 3 B, S6 & S7). This excludes gradual or localized exhumation by erosion or gravitational processes and technically qualifies them as input parameters for magnitude calculations after Wells and Coppersmith (1994). Minor error sources are misinterpretations of displacement per event, as ribbons may be defaced and overseen. When using fault lengths as input data for the Wells and Coppersmith (1994) method, incorrect recognition of the actual fault lengths constitutes a similar minor error source (see also Section 4.2.1; Table S9). The most severe error source, however, is the application of the empirical approach itself. For our setting with short fault lengths and relatively low magnitudes (i.e., M_w<6), Wells and Coppersmith (1994) only present limited data so that the adequacy of this statistical method is questionable. Depending on the of the interpretation of our NFS in a per se contractional setting (see Section 5.4), they may portray magnitudes ranging ca. 1 M below the actual magnitude evoked by the rupture of first order thrust faults. The obtained values would therefore advance to magnitudes in the range of the Montenegro 1979 earthquake, which are likelier to produce crustal ruptures of such scale (e.g., McCalpin, 1996).

5.4. Formation mechanisms of normal fault scarps

The position of the NFSBFS and KFS in the hinge of thrust-related anticlines within the nappe stack of the Kruja-Dalmatian Unit suggests their possible origin along pre-existing planes of weakness (fold-related longitudinal fractures, e.g., Ramsay and Huber, 1983; Tavani et al., 2015 *and references therein*). Two hypotheses are invoked to explain the NFStheir formation in an area governed by horizontal shortening: (i) The northward-migrating boundary between foreland contraction and hinterland extension, which has increasingly migrated westward since Late Eocene (e.g., Dumurdzanov et al., 2005; Reicherter et al., 2011; Handy et al., 2019). (ii) The activation of normal faults as second-order structures during rupture of subjacent first order thrust faults (e.g., Hicks and Rietbrock, 2015), where strain is partitioned in the upper plate or hanging wall. (ii) The northwestward migrating boundary between foreland contraction and hinterland extension, which has increasingly migrated westward since the Late Eocene (e.g., Dumurdzanov et al., 2005; Reicherter et al., 2011; Handy et al., 2019). Recent geodetic studies show that the working area lies in the frontalmost part of the deformation zone, right at the tip of a north-westwards propagating line separating hinterland extension from foreland contraction (Figs. 1 & 9 B, D'Agostino et al., 2021).

Gravitational collapse as a result of potential energy contrasts (sensu Copley et al., 2009) can be ruled out as striations, although diverging outward, are relatively consistent with respect to the undulating but otherwise planar fault planes.

1 & 9 B; D'Agostino et al., 2021). Furthermore, the existence of the described NFS has implications on observed GPS-derived convergence rates: The fault slip rate of 1.5 mm/yr along the normal fault plane with a dip of 60° results in a horizontal extension of 0.75 mm/yr. In order to achieve the geodetically observed convergence of 3-4 mm/yr, the actual convergence must therefore be 3.75-4.75 mm/yr (Fig.- 9 D). The accommodation of the total convergence in the coastal area (Fig. 9 C) and the lack of instrumentally recorded extensional earthquakes are strongly supportive of scenario (iii). This is further substantiated by the existence of other recent geomorphological features in the study area such as dry valleys and deflected river channels, which indicate a still predominantly contractional regime (Fig. 10, Biermanns et al., 2019; Schmitz et al., 202010; Biermanns et al., 2019; Schmitz et al., 2020). The formation of the NFS in consequence of gravitational collapse, i.e., landsliding, can be ruled out. (i) To our knowledge, it has never been reported or proven that landslides create a comparable geomorphic landscape with large-scale surface ruptures/fault planes in a similarly complex array (i.e., largely consistent overall characteristics of the rupture, despite changing orientation, bedrock and several apparent 'gaps'). Instead, exactly these characteristics apply to other verified examples of seismogenic NFS (e.g., Mason et al. 2016, 2017, a study that is probably best-comparable in terms of bedrock, fault scarp and slope morphology). (ii) The same is valid for the slickenside striations on ~10 m high(!) free faces that – although slightly diverging outward – are almost consistent with respect to the undulating but otherwise planar fault planes. (iii) No convincing (geomorphic) features typical of landsliding have been identified in the surroundings of the NFS (for comparison, e.g. Highland and Bobrowski, 2008). Large portions of the hanging wall, particularly along the eastern ends of BFS_S and KFS are clearly lacking any potential landslide deposits (i.e., quaternary/colluvium deposits; Fig. 4a). (iv) Neither the described earthquake-related ribbons, nor the mapped transfer faults or the western termination of KFS (indicative of strike-slip motion; see end of Section 4.1) are compatible with a landsliding-related origin. (v) The described transition of BFS_N into BFS_S features fault traces in bare rock forming relays. (vi) The presented setting is assessed to be scarcely landslide-prone with its barely water-saturated massive limestone bedrock and unhampered runoff (as particularly underpinned by the pronounced gullies across the NFS).

6. Conclusion

We report two previously unknown, active normal faults with well-preserved bedrock NFS along the contractional front of the southern Dinarides fold and thrust-belt. We propose a tectonic, co-seismic origin of these structures. Relations between fault orientation, striations, earthquake ribbons and surrounding structures suggest that the normal faults are either the result of rollback-induced westward migrating extensional tectonics or more likely second-order features linked to subjacent, higher-order thrusts, capable of triggering earthquakes up to $M_w≈7± ±$ 0.5. Maximum magnitudes ^{36}Cl cosmogenic dating for one sampling site on the NFS are expected to reach $M_w≈6±0.5$. Long-term fault slip rates were estimated from free-face height and height of the degraded scarp, assumingsuggests a post-LGM formation age (≤18 with significant free face development starting (or resuming) around 6 kyr~~)~~ ago. It is stressed that the provided date marks the onset of fault scarp formation (i.e., surficial manifestation toward the present state) but not necessarily the initial onset of ~~the NFS. Minimum~~activity on the fault(s). An annual slip rate of 1.5 ± 0.1 mm is released in 6 - 15 cm steps during earthquakes with recurrence intervals estimated to 35-100 yrs. To name an absolute lower limit in terms of slip rates, we calculated sets of qualitative slip-rates based on fault scarp profiles at four selected ~~sites amount~~locations. Normalised to a full post-LGM period of 18 ± 3 kyr (e.g., Papanikolaou et al., 2005), this method yields minimum slip rates of 0.34 ± 0.1 ~~-~~to 0.49 ± 0.1 mm/yr and recurrence intervals for major earthquakes ~~are~~ in the range of ≤400 yrs. Although ~~site selection has a large effect on final estimates,~~ these values theoretically quantify the overall fault activity, the faults are better characterised as structures where slip clustering leads to alternating high-activity and quiescence phases. Altogether, all of the presented values appear realistic against the backdrop of available GPS rates and common earthquake magnitudes in the region. The normal faults are exactly located above the "blind" thrust fault and epicentre that was responsible for the M_w 7.1 Montenegro 1979 earthquake, and hence suggest a relation. In any case, we regard the NFS as a manifestation of repeated earthquake activity in the study area.

Author ~~contributionss~~contributions

Peter Biermanns: Field work, data processing, methodology, original draft preparation, figure visualisation, coordination of writing and editing process, investigation.

Benjamin Schmitz: Field work, data processing, methodology, review and editing, figure visualisation, investigation.

Silke Mechernich: Field work, laboratory analyses, age modelling, writing, review and editing.

Christopher Weismüller: Field work, data processing, figure visualization.

Kujtim Onuzi: Resources, supervision.

Kamil Ustaszewski: Conceptualisation, supervision, project administration, funding acquisition, review and editing.

Klaus Reicherter: Conceptualisation, supervision, project administration, funding acquisition, review and editing.

Competing interests

The authors declare that they have no conflict of interest.

Data ~~availabilty~~availability

All essential data that this research article is based on are displayed in the according text, figures and supplementary material. Further raw data is available from the corresponding author on reasonable request.

~~Acknowlegdements~~

Acknowledgements

We cordially thank Kristijan Sokol, Martin Đaković and Rosalie Kremser for their help with field work, logistics and data processing. The German Aerospace Center (DLR) is thanked for the complimentary provision of TanDEM-X digital elevation data. The very constructive in-depth review of Gerald Roberts greatly enhanced the quality of this paper. The review of Lucilla Benedetti significantly contributed to an improved structure and clearer storyline. Project ALMOND was financed by Deutsche Forschungsgemeinschaft (DFG, project no. 269913092) granted to Klaus Reicherter and Kamil Ustaszewski.

References

Allen, J.R.M., Brandt, U., Brauer, A., Hubberten, H.W., Huntley, B., Keller, J., Kraml, M., Mackensen, A., Mingram, J., Negendank, J.F.W., Nowaczyk, N.R., Oberhansli, H., Watts, W.A., Wulf, S., Zolitschka, B.: Rapid environmental changes in southern Europe during the last glacial period, Nature 400, 740–743, 1999.

Armijo, R., Lyon-Caen, H. and Papanastassiou, D.: East-west extension and Holocene normal-fault scarps in the Hellenic arc, Geology, 20, 491-494, 1992.

Avouac, J.P., Meyer, B., Tapponier, P.: On the growth of normal faults and the existence of flats and ramps along the El Asnam active fold and thrust system, Tectonics, 11 (1), 1992.

Battaglia, M., Murray, M. H., Serpelloni, E., Bürgmann, R.: The Adriatic region: An independent microplate within the Africa-Eurasia collision zone, Geophys. Res. Lett. 31(9), 2004.

Beck, J., Wolfers, S., Roberts, G. P.: Bayesian earthquake dating and seismic hazard assessment using chlorine-36 measurements (BED v1), Geosci. Model Dev., 11(11), 4383-4397, 2018.

Benedetti, L., Finkel, R., Papanastassiou, D., King, G., Armijo, R., Ryerson, F., Farber, D. and Flerit, F.: Post-glacial slip history of the Sparta fault (Greece) determined by 36 Cl cosmogenic dating: Evidence for non-periodic earthquakes, Geophys. Res. Lett., 29 (8), doi: 10.1029/2001GL014510, 2002.

Benedetti, L., Manighetti, I., Gaudemer, Y., Finkel, R., Malavieille, J., Pou, K., Arnold, M., Aumaître, G., Bourlès, D., Keddadouche, K.: Earthquake synchrony and clustering on Fucino faults (Central Italy) as revealed from in situ ^{36}Cl exposure dating, J. Geophys. Res. Solid Earth, 118 (9), 4948-4974, 2013.

Benetatos, C. and Kiratzi, A.: Finite-fault slip models for the 15 April 1979 (Mw 7.1) Montenegro earthquake and its strongest aftershock of 24 May 1979 (Mw 6.2), Tectonophysics, 421, 129-143, 2006.

Bennett, R.A., Serpelloni, E., Hreinsdóttir, S., Brandon, M.T., Buble, G., Basic, T., Casale, G., Cavaliere, A., Anzidei, M., Marjonovic, M., Minelli, G., Molli, G., Montanari, A.: Syn-convergent extension observed using the RETREAT GPS network, northern Apennines, Italy, J. Geophys. Res. Solid Earth, 117 (B4), 2012.

Biermanns, P., Schmitz, B., Ustaszewski, K. and Reicherter, K., Tectonic geomorphology and Quaternary landscape development in the Albania – Montenegro border region: An inventory, Geomorphology, 326, 116-131, 2019.

Benetatos, C. and Kiratzi, A.: Finite-fault slip models for the 15 April 1979 (Mw 7.1) Montenegro earthquake and its strongest aftershock of 24 May 1979 (Mw 6.2), Tectonophysics, 421, 129-143, 2006.

Bubeck, A., Wilkinson, M, Roberts, G.P., Cowie, P.A., McCaffrey, K.J.W., Phillips, R. and Sammonds, P.: The tectonic geomorphology of bedrock scarps on active normal faults in the Italian Apennines mapped using combined ground penetrating radar and terrestrial laser scanning, Geomorphology, 237, 38-51, 2015.

Carminati, E. and Doglioni, C.: Alps vs. Apennines: The paradigm of a tectonically asymmetric Earth, Earth Sci. Rev., 112, 67-96, 2012.

Cavinato, G.P. and De Celles, P.G.: Extensional basins in the tectonically bimodal central Apennines fold-thrust belt, Italy: Response to corner flow above a subducting slab in retrograde motion, Geology, 27(10), 955-958, 1999.

Chiaraluce, L. et al.: The 2016 Central Italy Seismic Sequence: A First Look at the Mainshocks, Aftershocks, and Source Models, Seismol. Res. Lett., 88 (3), 757-771, 2017.

Civico, R., Pucci, S., Villani, F., Pizzimenti, L., De Martine, P.M., Nappi, R. and the Open EMERGEO Working group: Surface ruptures following the 30 October 2016 M_w 6.5 Norcia earthquake, central Italy, J. Maps, 14(2), 151-160, 2018.

Copley, A., Boait, F., Hollingsworth, J., Jackson, J. and McKenzie, D.: Subparallel thrust and normal faulting in Albania and the roles of gravitational potential energy and rheology contrasts in mountain belts, J. Geophys. Res., 114, doi: 10.1029/2008JB005931, 2009.

Corrado, S., Aldega, L., Perri, F., Critelli, S., Muto, F., Schito, A., Tripodi, V.: Detecting syn-orogenic extension and sediment provenance of the Cilento wedge top basin (southern Apennines, Italy): Mineralogy and geochemistry of fine-grained sediments and petrography of dispersed organic matter, Tectonophysics, 750, 404-418, 2019.

Cowie, P.A., Phillips, R.J., Roberts, G.P., McCaffrey, K., Zijerveld, L.J.J., Gregory, L.C., Faure Walker, J., Wedmore, L.N.J., Dunai, T.J., Binnie, S.A., Freeman, S.P.H.T., Wilcken, K., Shanks, R.P., Huismans, R.S., Papanikolaous, I., Michetti, A.M., Wilkinson, M.: Orogen-scale uplift in the central Italian Apennines drives episodic behaviour of earthquake faults. Sci. Rep., 7 (1), 1-10, 2017.

D'Agostino, N., Avallone, A., Cheloni, D., D'Anastasio, E., Mantenuto, S. and Selvaggi, G.: Active tectonics of the Adriatic region from GPS and earthquake slip vectors, J. Geophys. Res., 113, B12413, doi: 10.1029/2008JB005860, 2008.

Devoti, R., D'Agostino, N., Serpelloni, E., Pietrantonio, G., Riguzzi, F., Avallone, A., Cavaliere, A., Cheloni, D., Cecere, G., D'Ambrosio, C., Falco, L., Selvaggi, G., Métois, M., Esposito, A., Sepe, V., Galvani, A., and Anzidei, M.: A Combined Velocity Field of the Mediterranean Region, Annals of Geophysics,Ann. Geophys., 60 (2), S0217, doi:0210.4401/ag-7059, 2017.

D'Agostino, N., Métois, M., Koci, R., Duni, L., Kuka, N. Ganas, A., Georgiev, I., Jouanne, F., Kaludjerovic, N., Kandić, R., Active crustal deformation and rotations in the southwestern Balkans from continuous GPS measurements, Earth and Planetary Science Letters,& Planet. Sci. Lett., Vol. 539, https://doi.org/10.1016/j.epsl.2020.116246, 2020.

Dramis, F., Blumetti, A.M.: Some considerations concerning seismic geomorphology and paleoseismology. Tectonophysics, 408(1-4), 177-191, 2005.

Dumurdzanov, N., Serafimovski, T. and Burchfiel, B.C.: Cenozoic tectonics of Macedonia and its relation to the South Balkan extensional regime, Geosphere, 1, 1-22, 2005.

Faccenna, C., Becker, T. W., Auer, L., Billi, A., Boschi, L., Brun, J. P., Capitanio, F. A., Funiciello, F., Horvàth, F., Jolivet, L., Piromallo, C., Royden, L., Rossetti, F., and Serpelloni, E.: Mantle dynamics in the Mediterranean, Reviews of Geophysics,Rev.Geophys. 52 (3), 283-332, 2014.

Faure Walker, J., Roberts, G. P., Cowie, P. A., Papanikolaou, I. D., Sammonds, P. R., Michetti, A. M., Phillips, R. J.: Horizontal strain-rates and throw-rates across breached relay zones, central Italy: Implications for the preservation of throw deficits at points of normal fault linkage, J.Struct. Geol., 31 (10), 1145-1160, 2009.

Galadini, F. and Galli, P.: Active tectonics in the central Apennines (Italy)–input data for seismic hazard assessment, NaturalNat. Hazards, 22.3, 225-268, 2000.

Geological Survey of Montenegro: BasicGeological map of Montenegro, 1:25k geological map sheet of Yugoslavia 1:100.000, sheet Bar (K34-75), FederalVladimir 160-4-3 and 1:50k geological Institute, Beograd, 1971map sheet Podgorica 3, 2009.

Giraudi, C.: Considerations on the significance of some postglacial fault scarps in the Abruzzo Apennines (Central Italy), Quat. Int. 25, 33– 45, 1995.

Giraudi, C. and Frezzotti, M.: Paleoseismicity in the Gran Sasso Massif (Abruzzo, Central Italy), Quat. Int., 25, 81-93, 1995.

Giraudi, C., Frezzotti, M.: Late Pleistocene glacial events in the central Apennines, Italy, Quat. Res. 48, 280–290, 1997.

Goldberg, R., Siman-Tov, S. and Emmanuel, S.: Weathering resistance of carbonate fault mirrors promotes rupture localization, Geophys. Res. Lett., 43, 3105-3111, 2016.

Goodall, H.J., Gregory, L.C., Wedmore, L.N.J., MacCaffrey, K.J.W., Amey, R.M.J., Roberts, G.P., Shanks, R.P., Phillips, R.J., Hooper, A.: Determining Histories of Slip on Normal Faults with Bedrock Scarps Using Cosmogenic Nuclide Exposure Data, Tectonics 40(3), 2021.

Grünthal, G., Wahlstrom, R. and Stromeyer, D.: The SHARE European -Earthquake Catalogue -(SHEEC) -for -the -Time Period -1900-2006 -and -Its -Comparison -to -the EuropeantheEuropean-Mediterranean -Earthquake -Catalogue -(EMEC), J. Seismol. 17, 1339-1344, 2013.

Grützner, C., Barba, S., Papanikolaou, I. and Pérez-López, R.: Earthquake geology: science, society and critical facilities, Ann. Geophys., 56(6), 2013.

Grützner, C., Schneiderwind, S., Papanikolaou, I., Deligiannakis, G., Pallikarakis, A. and Reicherter, K.: New constraints on extensional tectonics and seismic hazard in northern Attica, Greece: the case of the Milesi Fault, Geophys. J. Int., 204, 180-199, 2016.

Handy, M.R., Ustaszewski, K., Kissling, E.: Reconstructing the Alps-Carpathians-Dinarides as a key to understanding switches in subduction polarity, slab gaps and surface motion. Int. J. Earth Sci. 104(1), 1–26, 2015.

Handy, M. R., Giese, J., Schmid, S. M., Pleuger, J., Spakman, W., Onuzi, K., and Ustaszewski, K.: Coupled Crust-Mantle Response to Slab Tearing, Bending, and Rollback Along the Dinaride-Hellenide Orogen, Tectonics, 38, 2803-2828, 2019.

Hicks, S. P., and Rietbrock, A.: Seismic slip on an upper-plate normal fault during a large subduction megathrust rupture, ~~Nature Geoscience,~~Nat. Geosci., 8, 955, 2015.

Highland, L., Bobrowsky, P.T.: The landslide handbook: a guide to understanding landslides, Reston: US Geological Survey, 2008.

Hunstad, I., Selvaggi, G., D'Agostino, N., England, P., Clarke, P. and Pierozzi, M.: Geodetic strain in peninsular Italy between 1875 and 2001, Geophys. Res. Lett., 30(4), 2003.

Iezzi, F., Roberts, G., Faure Walker, J., Papanikolaou, I., Ganas, A., Deligiannakis, G., Beck, J., Wolfers, S., Gheorghiu, D.: Temporal and spatial earthquake clustering revealed through comparison of millennial strain-rates from 36Cl cosmogenic exposure dating and decadal GPS strain-rate, Sci. Rep., 11(1), 1-12, 2021.

Jouanne, F., Mugnier, J.L., Koci, R., Bushati, S., Matev, K., Kuka, N., Shinko, I., Kociu, S., Duni, L.: GPS constraints on current tectonics of Albania, Tectonophysics 554, 50-62, 2012.

Király, Á., Faccenna, C., and Funiciello, F.: Subduction Zones Interaction Around the Adria Microplate and the Origin of the Apenninic Arc, Tectonics, 37, 3941-3953, https://doi.org/10.1029/2018TC005211, 2018.

Kuhlemann, J., Milivojević, M., Krumrei, I. and Kubik, P.W.: Last glaciation of the Šara range (Balkan peninsula): Increasing dryness from the LGM to the Holocene, Austrian J. Earth Sci., 102, 146-158, 2009.

Le Breton, E. Handy, M.R., Molli, R., Ustaszewski, K.: Post-20 Ma Motion of the Adriatic Plate: New Constraints From Surrounding Orogens and Implications for Crust-Mantle Decoupling. Tectonics, 36, 3135-3154, 2017

Mason, J., Schneiderwind, S., Pallikarakis, A., Wiatr, T., Mechernich, S., Papanikolaou, I. and Reicherter, K.: Fault structure and deformation rates at the Lastros-Sfaka Graben, Crete, Tectonophysics, 683, 216-232, 2016.

Mason, J., Schneiderwind, S., Pallikarakis, A., Mechernich, S., Papanikolaou, I., Reicherter, K.: Hanging-wall colluvial cementation along active normal faults, Quat. Res. 88 (1), 39-59, 2017.

McCalpin, J. (ed.): Paleoseismology, Volume 62, Academic Press, 1996.

Mechernich, S., Schneiderwind, S., Mason, J., Papanikolaou, I.D., Deligiannakis, G., Pallikarakis, A., Binnie, S.A., Dunai, T.J. and Reicherter, K.: The seismic history of the Pisia fault (eastern Corinth rift, Greece) from fault plane weathering features and cosmogenic 36Cl dating, J. Geophys. Res. Solid Earth, 123, 4266–4284, 2018.

Mechernich, S., Dunai, T.J., Binnie, S.A., Goral, T., Heinze, S., Dewald, A., Schimmelpfennig, I., Keddadouche, K., Aumaître, G., Bourlès, D., Marrero, S., Wilcken, K., Simon, K., Fink, D., Phillips, F.M., Caffee, M.W., Gregory, L.C., Phillips, R., Freemann, S.P.H.T., Shanks, R.P., Sarıkaya, M.A., Pavetich, S., Rugel, G., Merchel, S., Akçar, N., Yesilyurt, S., Ivy-Ochs, S., Vockenhuber, C.: Carbonate and silicate intercomparison materials for cosmogenic ^{36}Cl measurements, Nucl. Inst. Methods Phys. Res., B 455, 250-259, 2019.

Nábělek, J.: Geometry and mechanism of faulting of the 1980 El Asnam, Algeria, earthquake from inversion of teleseismic body waves and comparison with field observations, J. Geophys. Res. Solid Earth, 90 (B14), 12713-12728, 1985.

Nocquet, J.M., Calais, E.: Geodetic measurements of crustal deformation in the Western Mediterranean and Europe, Pure Appl. Geophys. 161(3), 661–681, 2004.

Nocquet, J.M.: Present-day kinematics of the Mediterranean: A comprehensive overview of GPS results, Tectonophysics, 579, 220-242, 2012.

Palumbo, L., Benedetti, L., Bourles, D., Cinque, A., & Finkel, R.: Slip history of the Magnola fault (Apennines, Central Italy) from 36Cl surface exposure dating: evidence for strong earthquakes over the Holocene, Earth Planet. Sci. Let., 225 (1-2), 163-176, 2004.

Papadopoulos, G. A., Agalos, A., Carydis, P., Lekkas, E., Mavroulis, S., and Triantafyllou, I.: The 26 November 2019 Mw 6.4 Albania Destructive Earthquake, Seismol. Res. Lett., 91, 3129-3138, 2020.

Papanikolaou, I.D., Roberts, G.P. and Michetti, A.M.: Fault scarps and deformation rates in Lazio-Abruzzo, Central Italy: Comparison between geological fault slip-rate and GPS data, Tectonophysics, 408, 147-176, 2005.

Papanikolaou, I. D., and Roberts, G. P.: Geometry, kinematics and deformation rates along the active normal fault system in the southern Apennines: Implications for fault growth, J. Struct. Geol. 29 (1), 166-188, 2007.

Papanikolaou, I., Roberts, G.P., Deligiannakis, G., Sakellariou, A. and Vassilakis, E.: The Sparta Fault, Southern Greece: From segmentation and tectonic geomorphology to seismic hazard mapping and time dependent probabilities, Tectonophysics, 597, 85-105, 2013.

Philip, H., and Meghraoui, M.: Structural analysis and interpretation of the surface deformations of the El Asnam earthquake of October 10, 1980, Tectonics, 2 (1), 17-49, 1983.

Pondrelli, S., Salimbeni, S., Ekström, G., Morelli, A., Gasperini, P. and Vannucci, G.: The Italian CMT dataset from 1977 to the present: Phys. Earth Planet. Inter., 159, 286-303, 2006.

Ramsay, J. G. and Huber, M. I.: The techniques of Modern Structural Geology: Volume 2: Folds and Fractures, Academic Press, London, 1983.

Reicherter, K., Hoffmann, N., Lindhorst, K., Krastel, S., Fernández-Steeger, Grützner, C. and Wiatr, T.: Active basins and neotectonics: morphotectonics of the Lake Ohrid Basin (FYROM and Albania), Z. dt. Geowiss., 162 (2), 217-234, 2011.

Riesner, M., Bollinger, L., Hubbard, J., Guérin, C., Lefèvre, M., Vallage, A., Shah, C.B., Kandel, T.P., Haines, S., Sapkota, S. N.: Localized extension in megathrust hanging wall following great earthquakes in western Nepal, Sci. Rep. 11 (1), 1-18, 2021.

Roberts, G. P. and Michetti, A. M.: Spatial and temporal variations in growth rates along active normal fault systems: an example from The Lazio–Abruzzo Apennines, central Italy. J. Struct. Geol., 26 (2), 339-376, 2004

Schlagenhauf, A., Y. Gaudemer, Y., Benedetti, L., Manighetti, I., Palumbo, L., Schimmelpfennig, I., Finkel, R. and Pou, K.: Using in situ Chlorine-36 cosmonuclide to recover past earthquake histories on limestone normal fault scarps: a reappraisal of methodology and interpretations, Geophys. J. Int., 182, 36–72, 2010.

Schlagenhauf, A., Manighetti, I., Benedetti, L., Gaudemer, Y., Finkel, R., Malavieille, J., Pou, K.: Earthquake supercycles in Central Italy, inferred from 36Cl exposure dating, Earth Planet. Sci. Lett. 307 (3-4), 487-500, 2011.

Schmid, S. M., Fügenschuh, B., Kounov, A., Maţenco, L., Nievergelt, P., Oberhänsli, R., Pleuger, J., Schefer, S., Schuster, R., Tomljenović, B., Ustaszewski, K., and van Hinsbergen, D. J. J.: Tectonic units of the Alpine collision zone between Eastern

Alps and western Turkey, Gondwana Research, 78, 308-374, 2020.

Schmitz, B., Biermanns, P., Hinsch, R., Đaković, M., Onuzi, K., Reicherter, K. and Ustaszewski, K.: Ongoing shortening in the Dinarides fold-and-thrust belt: A new structural model of the 1979 (Mw 7.1) Montenegro earthquake epicentral region, J. Struct. Geol., 104192, 2020.

Schneiderwind, S., Boulton, S.J., Papanikolaou, I.D., Reicherter, K., 2017. Innovative tidal notch detection using TLS and fuzzy logic: Implications for palaeo-shorelines from compressional (Crete) and extensional (Gulf of Corinth) tectonic settings. Geomorphology, 283, 189-200.

Serpelloni, E., Facenna, C., Spada, G., Dong, D. and Williams, S.D.P.: Vertical GPS ground motion rates in the Euro-Mediterranean region: New evidence of velocity gradients at different spatial scales along the Nubia-Eurasia plate boundary, J. Geophys. Res. Solid Earth, 118, 6003-6024, 2013.

Stone, J. O., Allan, G. L., Fifeld, L.K. and Cresswell, R. G.: Cosmogenic chlorine-36 from calcium spallation, Geoch. Cosmochim. Acta, 60(4), 679-692, 1996.

Stone, J. O.: Air pressure and cosmogenic isotope production, J. Geophys. Res., 105, 23753 - 23759, 2000.

Tavani, S., Storti, F., Lacombe, O., Corradetti, A., Muñoz, J.A. and Mazzoli, S.: A review of deformation pattern templates in foreland basin systems and fold-and-thrust belts: Implications for the state of stress in the frontal regions of thrust wedges, Earth-Sci. Rev., 141, 82-104, 2015.

Tesson, J., Pace, B., Benedetti, L., Visini, F., Delli Rocioli, M., Arnold, M., Aumaître, G., Bourlès, D.L., Keddadouche, K.: Seismic slip history of the Pizzalto fault (central Apennines, Italy) using in situ-produced 36Cl cosmic ray exposure dating and rare earth element concentrations, J. Geophys.Res. Solid Earth, 121 (3), 1983-2003, 2016

Vittori, E., Blumetti, A. M., Comerci, V., Di Manna, P., Piccardi, L., Gega, D., and Hoxha, I.: Geological effects and tectonic environment of the 26 November 2019, Mw 6.4 Durres earthquake (Albania), ~~Geophysical Journal International,~~Geophys. J. Int., 225, 1174-1191, 2020.

Wells, D.L. and Coppersmith, K.J.: New empirical relationships among magnitude, rupture length, rupture width, rupture area, and surface displacement, B. Seismol. Soc. Am., 84 (4), 974-1002, 1994.

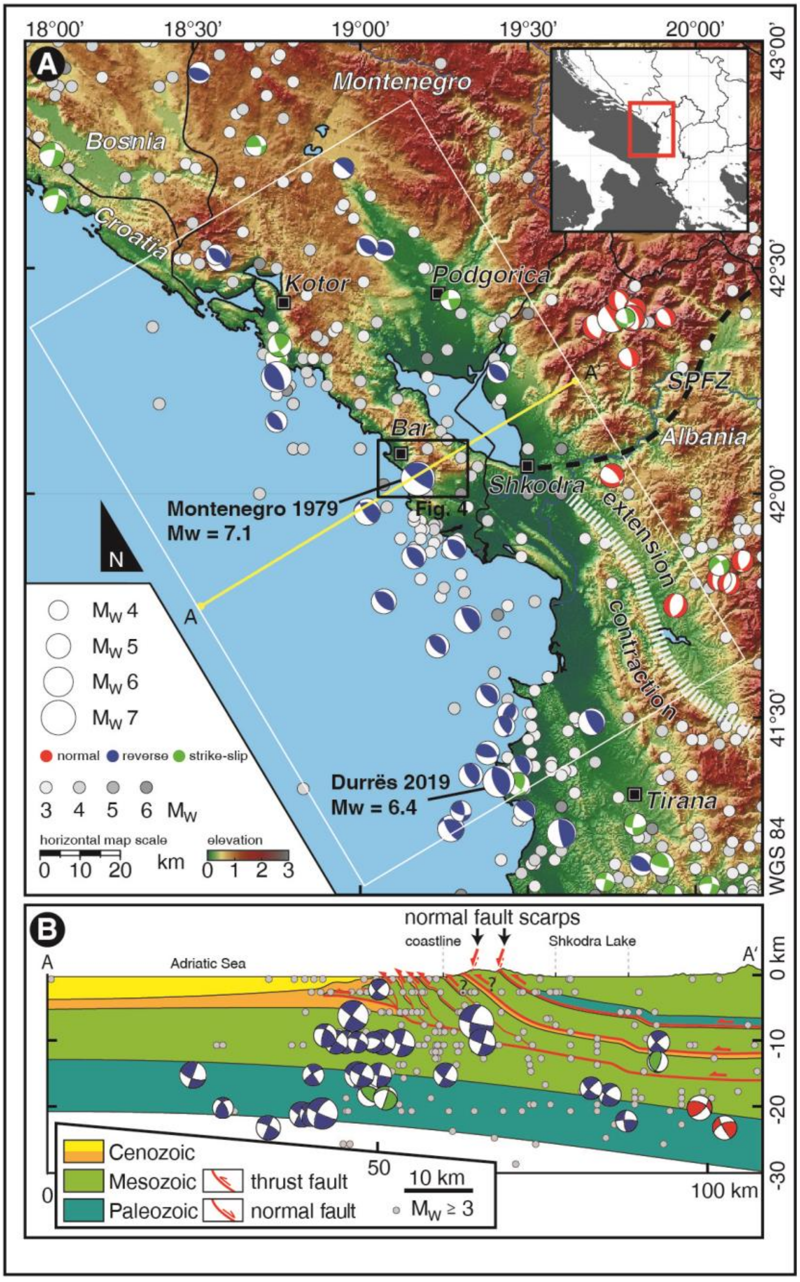

A
Montenegro
Bosnia
Croatia
Kotor
Podgorica
Bar
Shkodra
SPFZ
Albania
extension
contraction
Montenegro 1979
Mw = 7.1
Fig. 4
Durrës 2019
Mw = 6.4
Tirana
normal
reverse
strike-slip
horizontal map scale
elevation
km
WGS 84
B
normal fault scarps
coastline
Shkodra Lake
Adriatic Sea
Cenozoic
Mesozoic
Paleozoic
thrust fault
normal fault
10 km
100 km

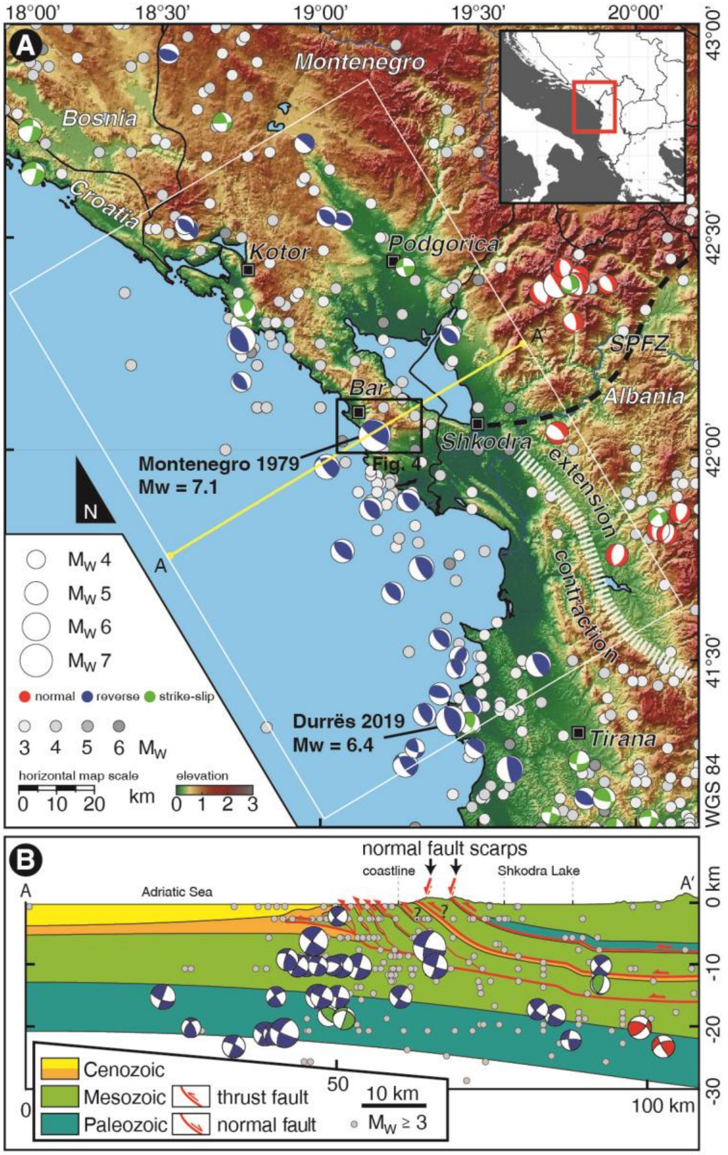

1405 **Figure 1: (a) Earthquakes in the study area: Where available, fault plane solutions (FPS) are scaled and color-coded according to magnitude and stress regime. All other earthquakes are color-coded by grey scales according to magnitude. SPFZ=Shkodra-Peja Fault Zone. (b) FPS projected onto Profile A-A' within the range of white box (Fig. 1A). FPS from EMSC, EMRCMT and Harvard catalogues, Pondrelli et al. (2006) and Grünthal et al. (2013).**

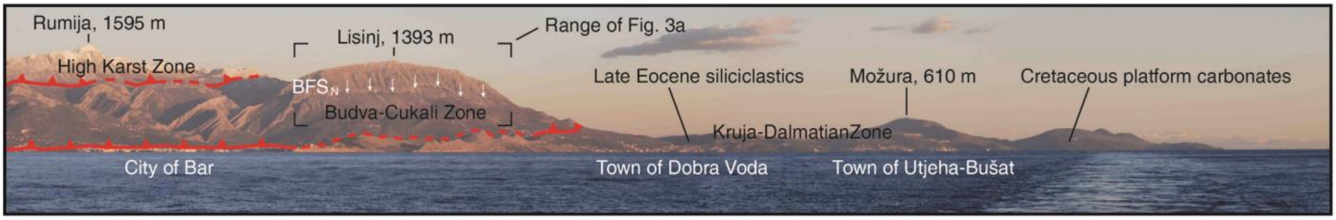

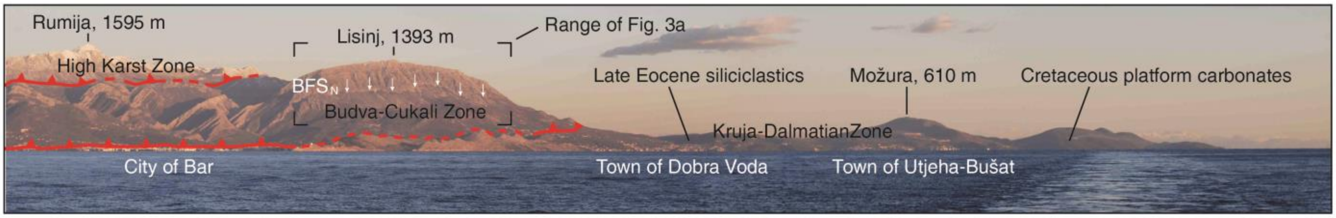

Figure 2: Panoramic view from aboard Meteor research vessel cruise No. 86, leg 3 SE towards the Montenegrin coast, including BFS$_N$. Basal thrusts separating the large-scale tectonic units and a choice of other landmarks are sketched.

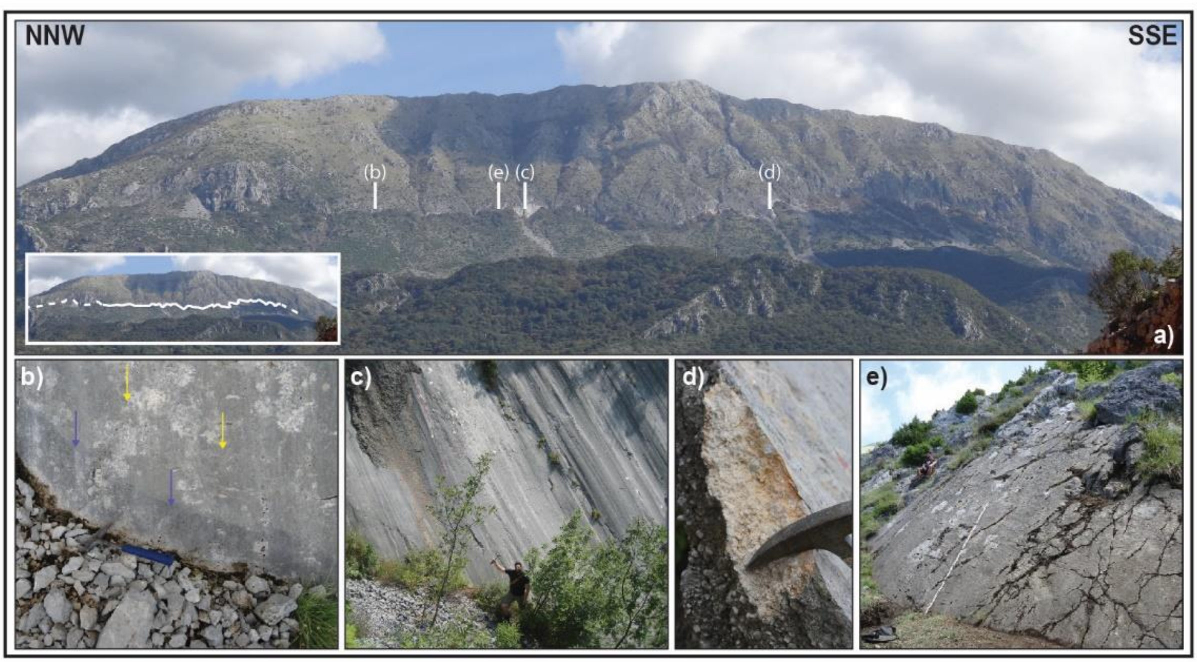

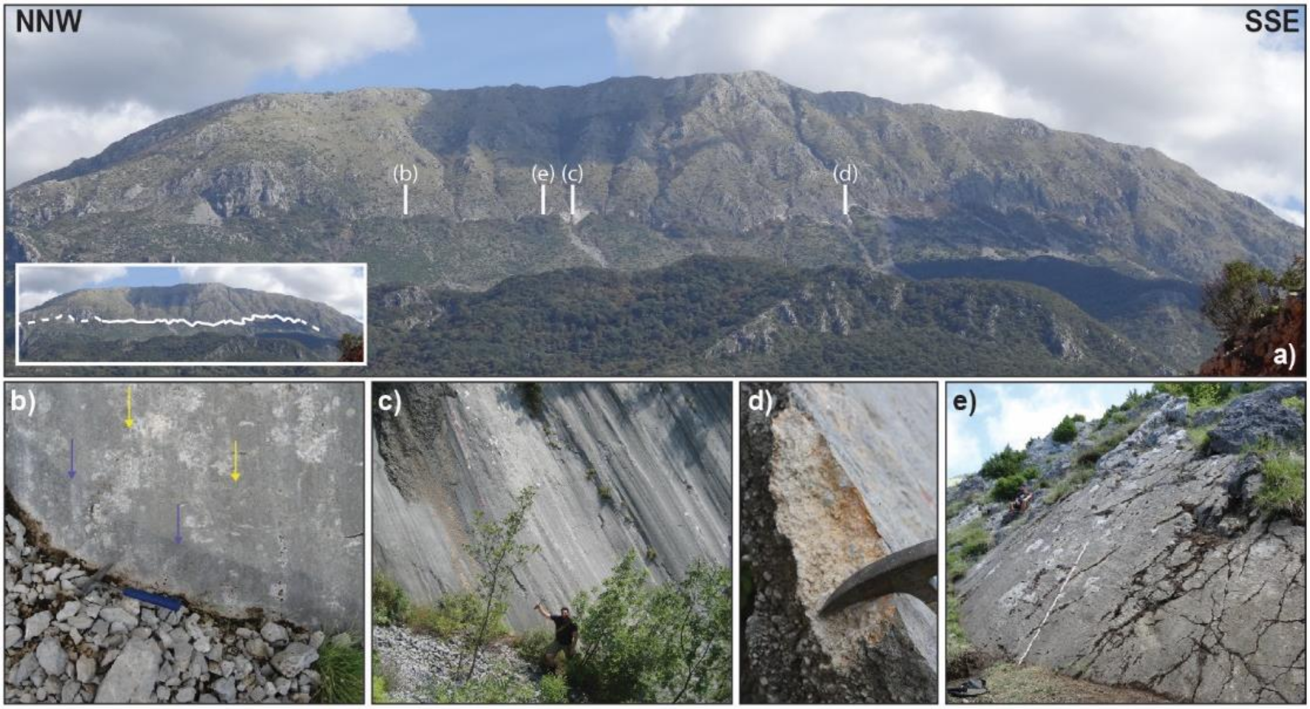

Figure 3: Photographs of the northern section of the Bar fault scarp (BFS$_N$): (A) Panoramic view, fault trace shown in inset. (B) Repeated earthquake ribbons; hammer for scale. Arrows: Blue=young; yellow=older. (C) Fault plane outcrop with characteristic corrugations and oblique-slip lineations; person for scale. (D) Cataclastic fault breccia in the footwall of fault plane; hammer for scale. (E) Sampling site BFS$_N$, 2-m ruler for scale; for localization see Fig. 4.

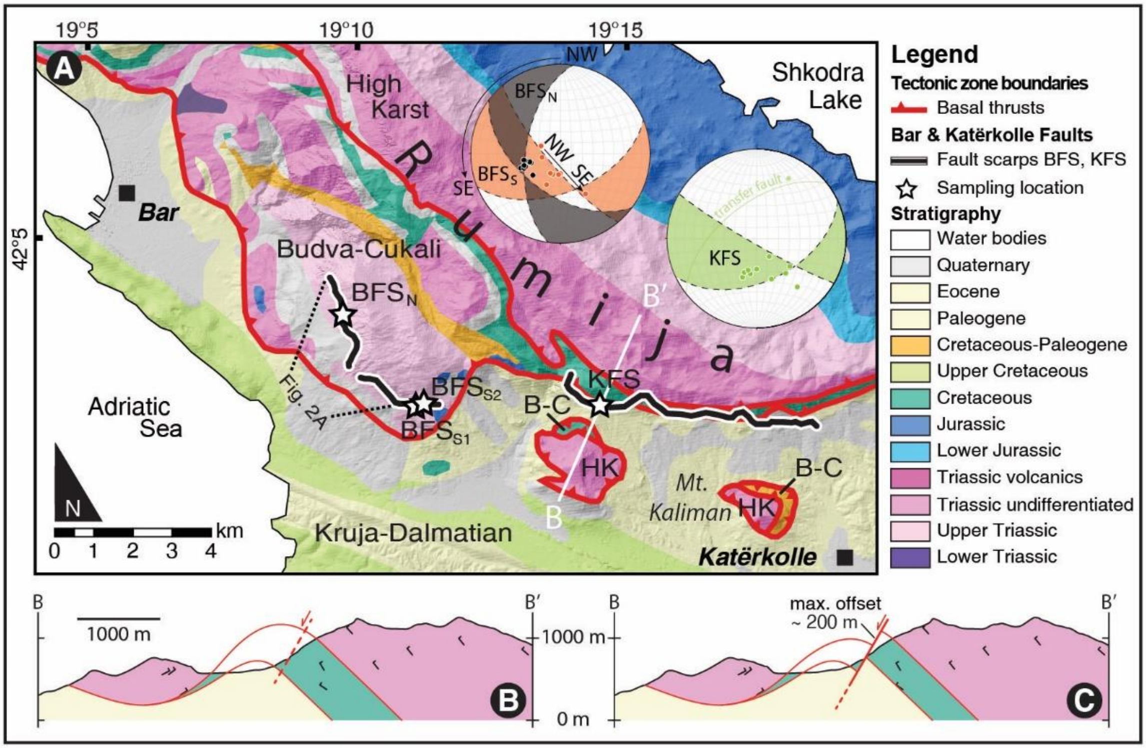

A
19°5
19°10
19°15
42°5
High Karst
Rumija
Budva-Cukali
Bar
Adriatic Sea
Kruja-Dalmatian
Shkodra Lake
Mt. Kaliman
Katërkolle
BFS_N
BFS_S2
BFS_S1
KFS
B-C
HK
B
B′
Fig. 2A
N
0 1 2 3 4 km
NW
SE
transfer fault
Legend
Tectonic zone boundaries
Basal thrusts
Bar & Katërkolle Faults
Fault scarps BFS, KFS
Sampling location
Stratigraphy
Water bodies
Quaternary
Eocene
Paleogene
Cretaceous-Paleogene
Upper Cretaceous
Cretaceous
Jurassic
Lower Jurassic
Triassic volcanics
Triassic undifferentiated
Upper Triassic
Lower Triassic
1000 m
1000 m
0 m
max. offset ~ 200 m
B
C

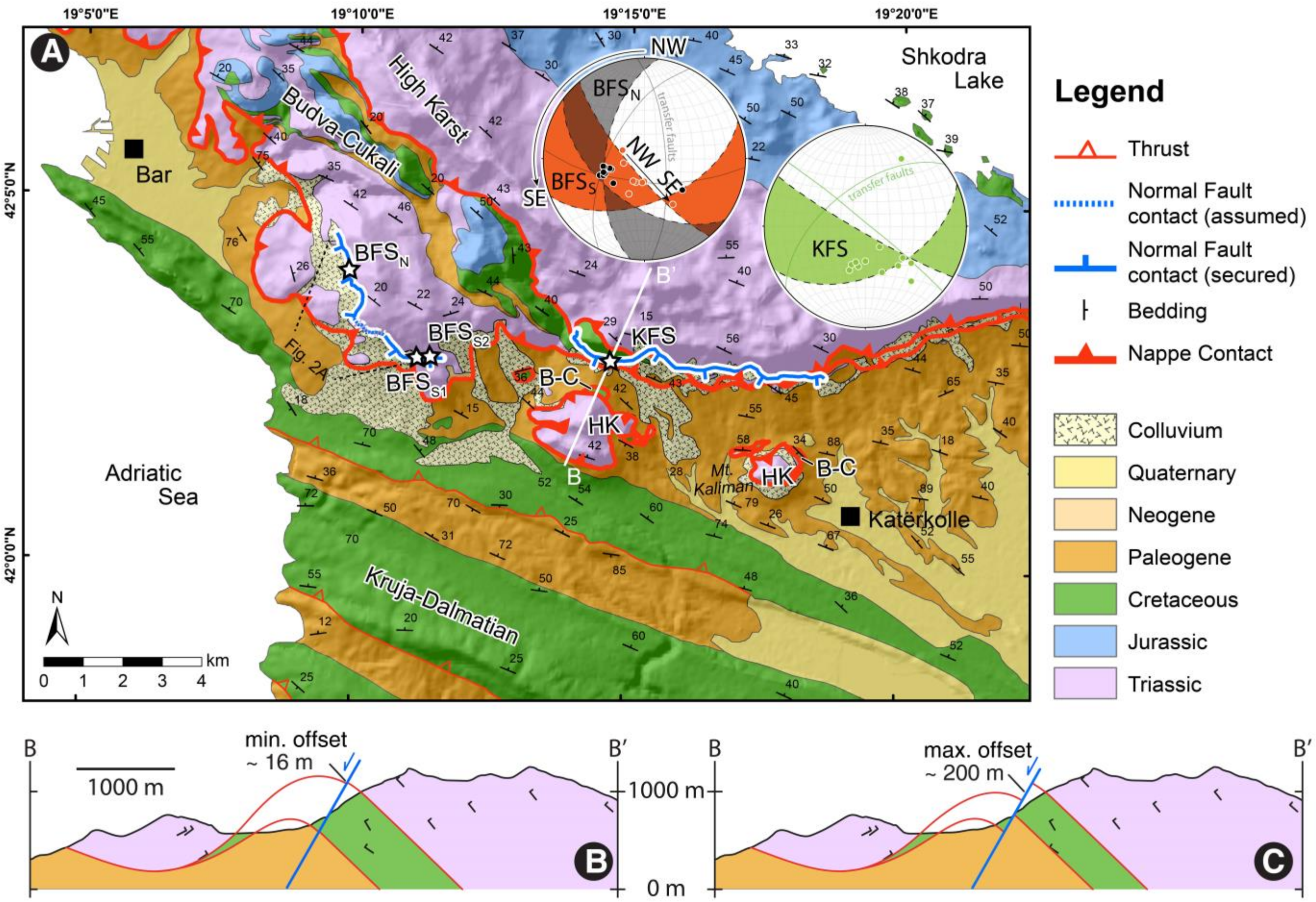

Figure 4: (A) Localization of BFS and KFS on athe geological map (compiled from the 1:25k geological map sheet Vladimir 160-4-3 and 1:50k geological map sheet Podgorica 3; Geological mapsurvey of Yugoslavia, 1971, map sheet Bar - K34-63.Montenegro, 2009). Stars indicate the sites of NFS profiles (Fig. 5). Stereoplots show orientations of the fault planeplanes and striations for BFS$_N$ (grey), BFS$_S$ (orange) and KFS (green); semitransparent coloringsemi-transparent colouring: range of main fault plane orientations; dots: mean striations. HK=orientations of the striation. Single great circles represent (i) smaller transfer faults that connect segments of the main fault plane and (ii) the fault branch at the western end of KFS. HK = High Karst, B-C= = Budva-Cukali. Bottom: Profile series across KFS indicating(B) Cross section showing the hypothetical minimum fault slip derived from the reconstructed visible fault scarp height at sampling site KFS (Fig. 5, bottom). (C) Cross section showing the proposed maximum fault slip, derived from the maximum offset by NFS; modified from Schmitz et al. (2020).of the Budva-Cukali marker between the outcrops at the Vladimir nappe outlier and the Rumija range.

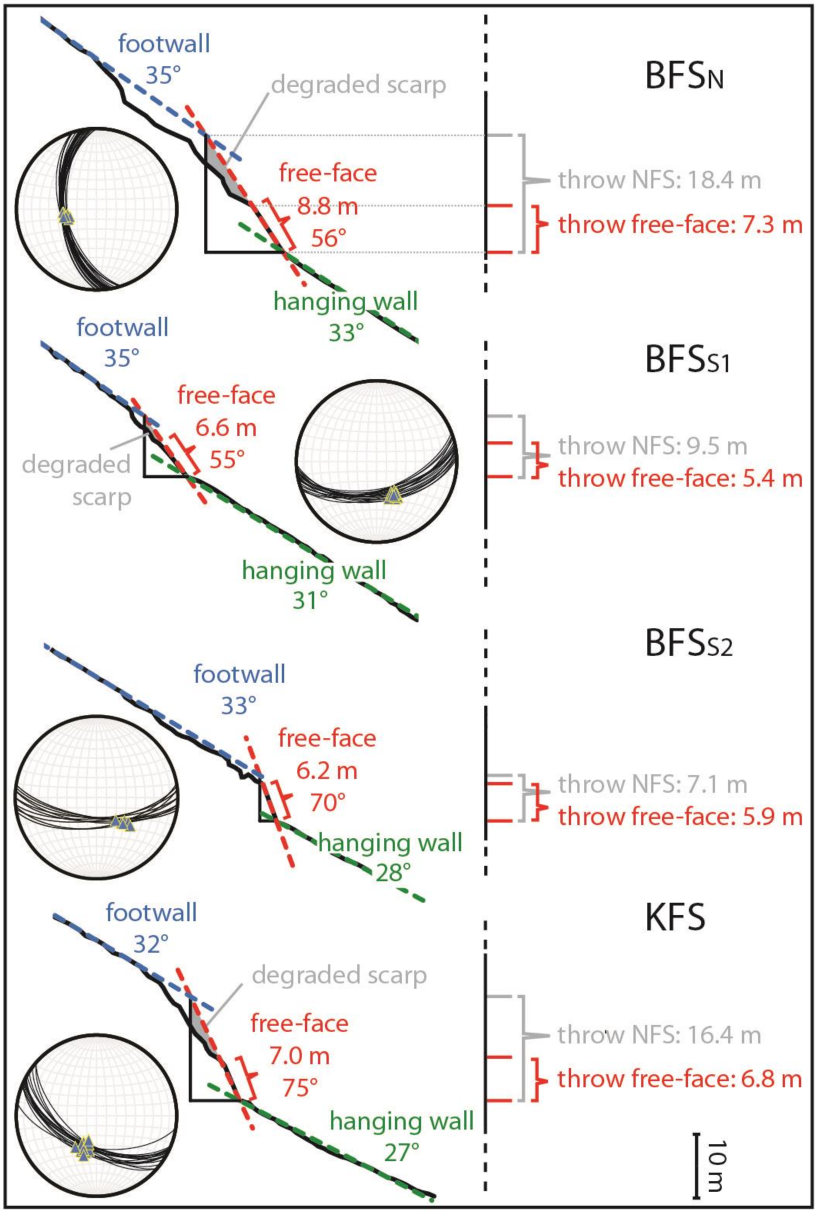

footwall
35°
degraded scarp
BFSN
free-face
8.8 m
56°
throw NFS: 18.4 m
throw free-face: 7.3 m
hanging wall
33°
footwall
35°
BFSS1
free-face
6.6 m
55°
degraded
scarp
throw NFS: 9.5 m
throw free-face: 5.4 m
hanging wall
31°
BFSS2
footwall
33°
free-face
6.2 m
70°
throw NFS: 7.1 m
throw free-face: 5.9 m
hanging wall
28°
footwall
32°
KFS
degraded scarp
free-face
7.0 m
75°
throw NFS: 16.4 m
throw free-face: 6.8 m
hanging wall
27°
10 m

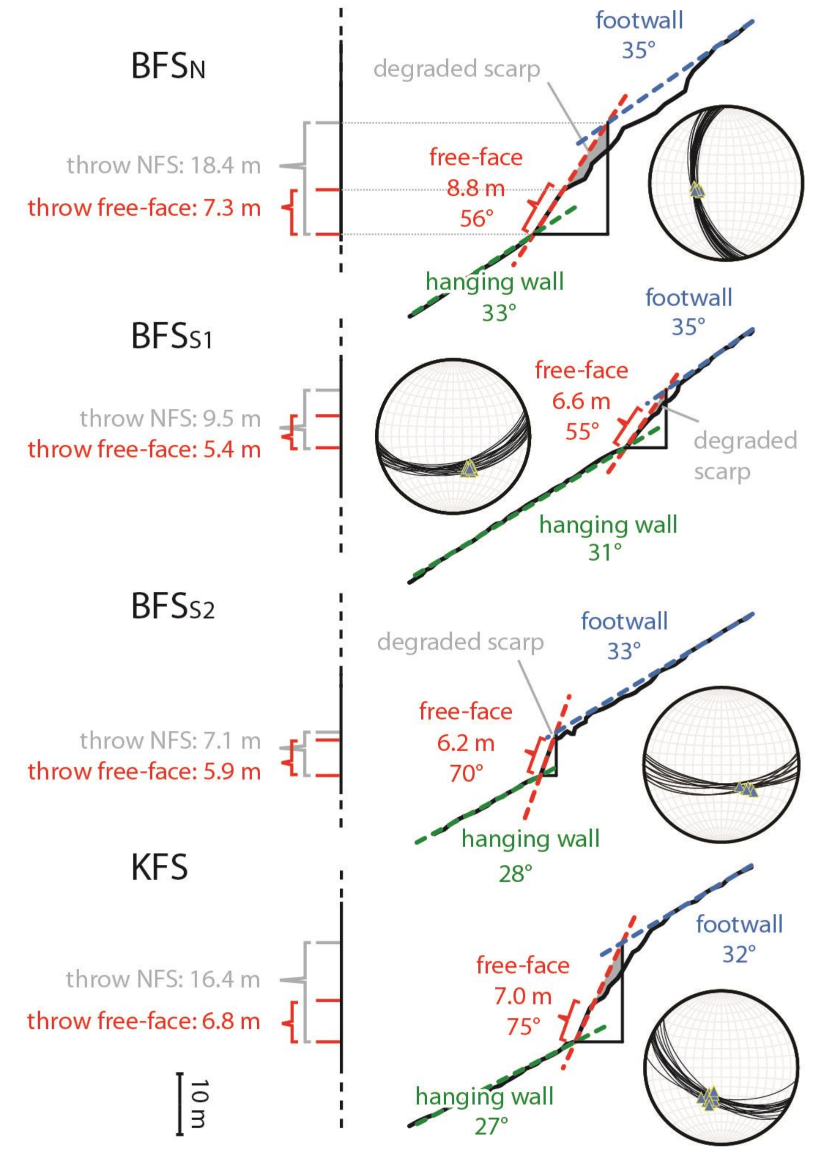

Figure 5: Profiles across the fault scarps at four selected sites (see Fig. 4 for locations). Slip rates are derived from the here presented free-face heights and heights including the degraded scarp (compare Table S10, two right columns). Stereoplots show fault plane orientations (great circles) and striations (triangles) within ± 5 m of the study site. Sites are indicated in Fig. 4; sites BFS$_N$ and BFS$_S$ are shown in Figs. 6 A – C & S2 C.

Figure 6: (A) Sampling location BFS_{S1} as an example where the criterion of a perfectly flat scarp base is met. (B) Difference between overgrown (top) and cleaned (bottom) fault plane at sampling location BFN_{N}. (C) Full view of the cleaned sampling location BFS_{N} including a trench below the scarp base. (D-F) Work in progress: Sample blocks are marked and extracted with the help of an angle grinder, hammer and chisel at sampling location BFS_{N}. Image F shows the trace of extracted sample blocks parallel to striations but avoiding disturbing factors such as joints.

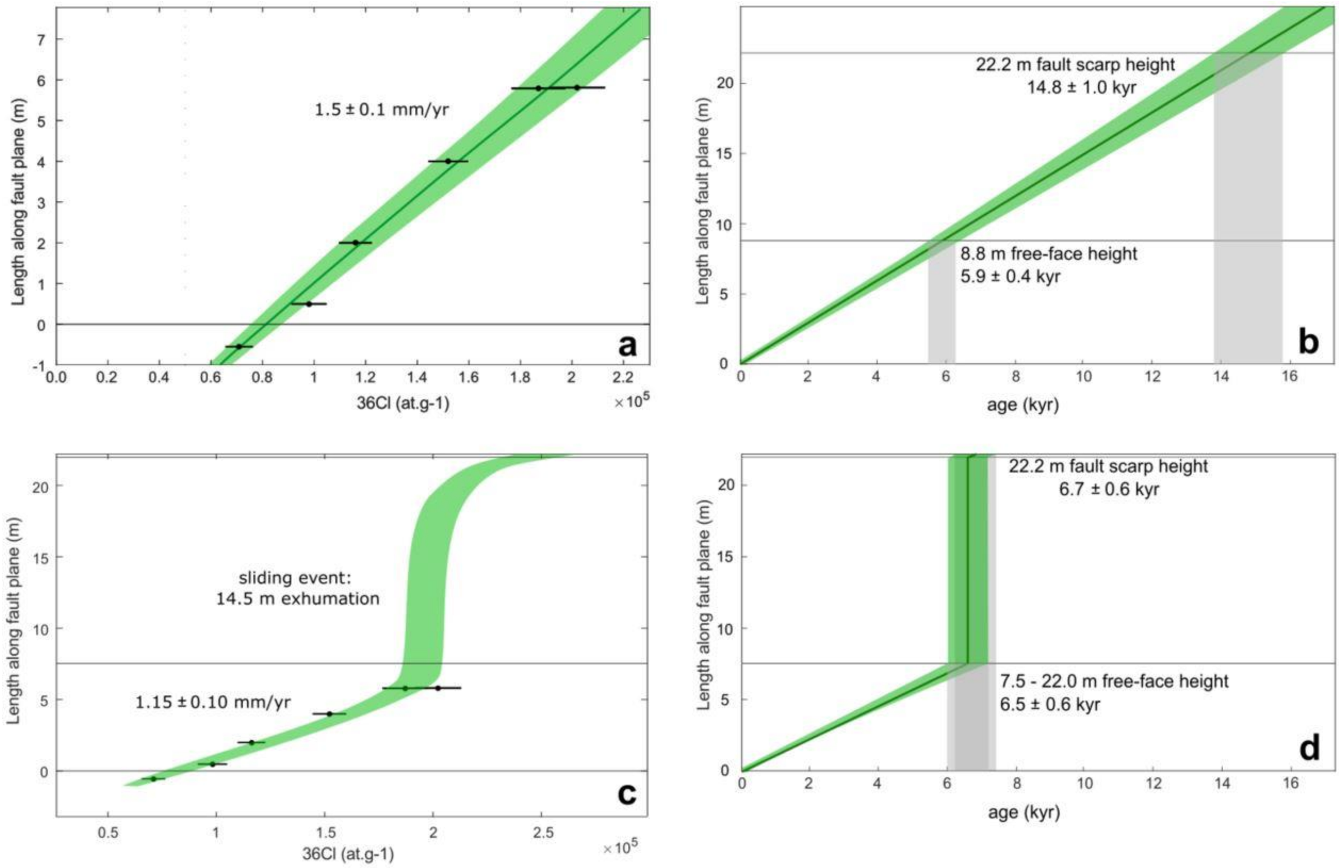

1.5 ± 0.1 mm/yr
Length along fault plane (m)
36Cl (at.g-1)
a
22.2 m fault scarp height
14.8 ± 1.0 kyr
8.8 m free-face height
5.9 ± 0.4 kyr
age (kyr)
b
sliding event:
14.5 m exhumation
1.15 ± 0.10 mm/yr
c
22.2 m fault scarp height
6.7 ± 0.6 kyr
7.5 - 22.0 m free-face height
6.5 ± 0.6 kyr
d

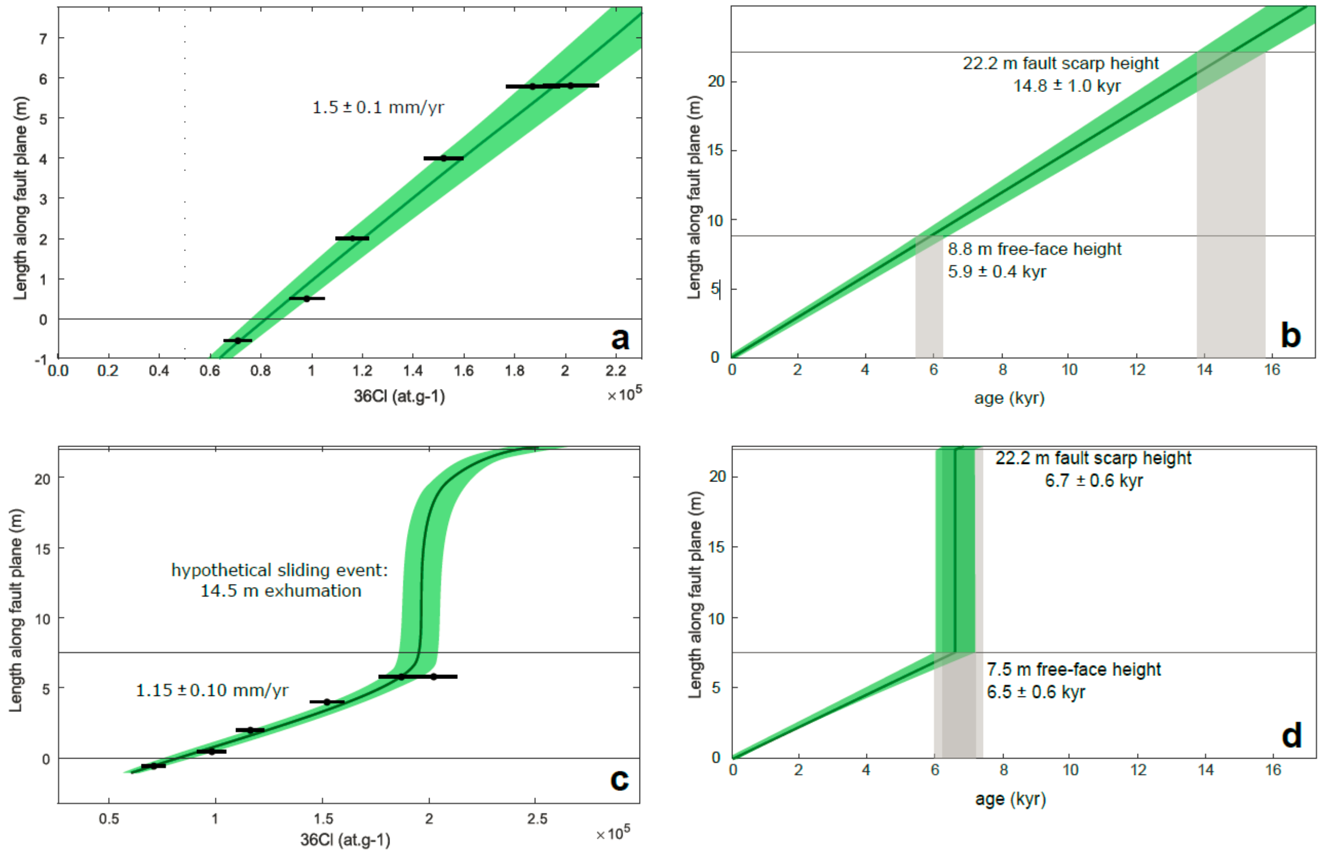

Figure 7: ^{36}Cl concentrations (1σ deviations) as a function of the height up the scarp (distance measured on the free-face). (A) Modelled ^{36}Cl concentrations for constant stick-slip rates (1.5 ± 0.1 mm/yr) using the code of Schlagenhauf et al. (2010), with the highest likelihood. (B) The resulting correlation of age and scarp height of (A). (C) Modelled 36Cl concentration for the ‘most ~~likely~~likely’ landslide/rockfall scenario. (D) The resulting correlation of age and scarp height of (B).

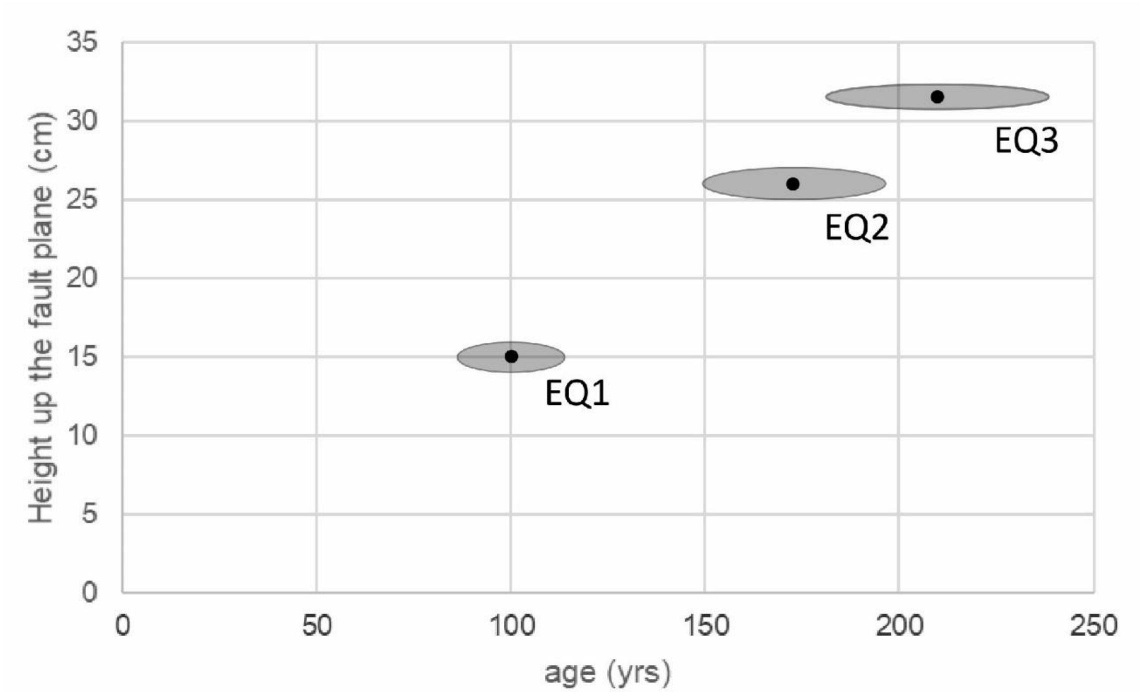

Figure 8: The exhumation history of the free-face at site BFS_N based on the modeling results (see Fig. 7 A & B). The slip rate of 1.7 ±0.1 mm/yr together with the coseismic amount of offset based on the mapped earthquake horizons results in earthquake ages of 100 ±14 yrs (EQ1), 173 ±24 yrs (EQ2) and 210 ±29 yrs (EQ3). All values are given within 68% (1 sigma) confidence interval.

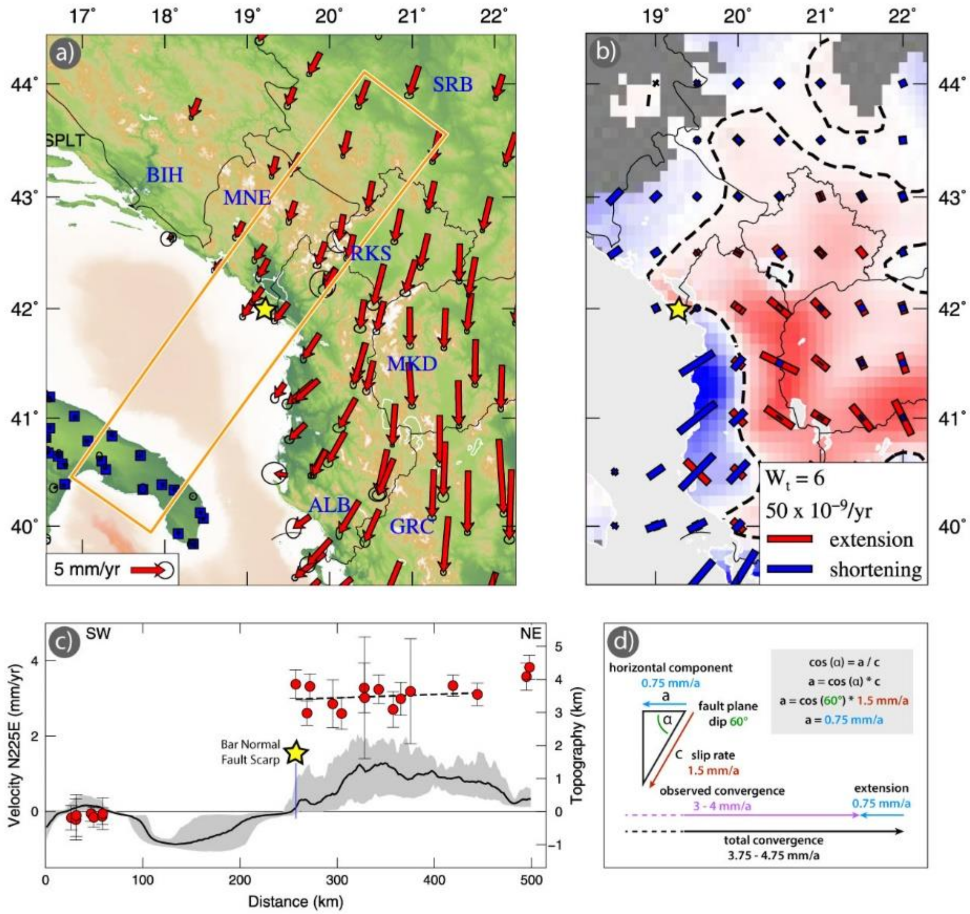

Figure 9: (a) Apulia referenced GPS velocity field and (b) interpolated strain rate with a Gaussian/Voronoi cell weighting of a net reweighting threshold of $W_t = 6$ in the southwestern Balkans. (c) Swath topographic section with GPS velocity information through the working area. ~~Figures~~Figs. (a)-(c) modified after and reprinted with permission from D'Agostino et al., 2020, see their work for details. (d) Normal faulting related horizontal velocity component and its accelerating role in cross-regional convergence.

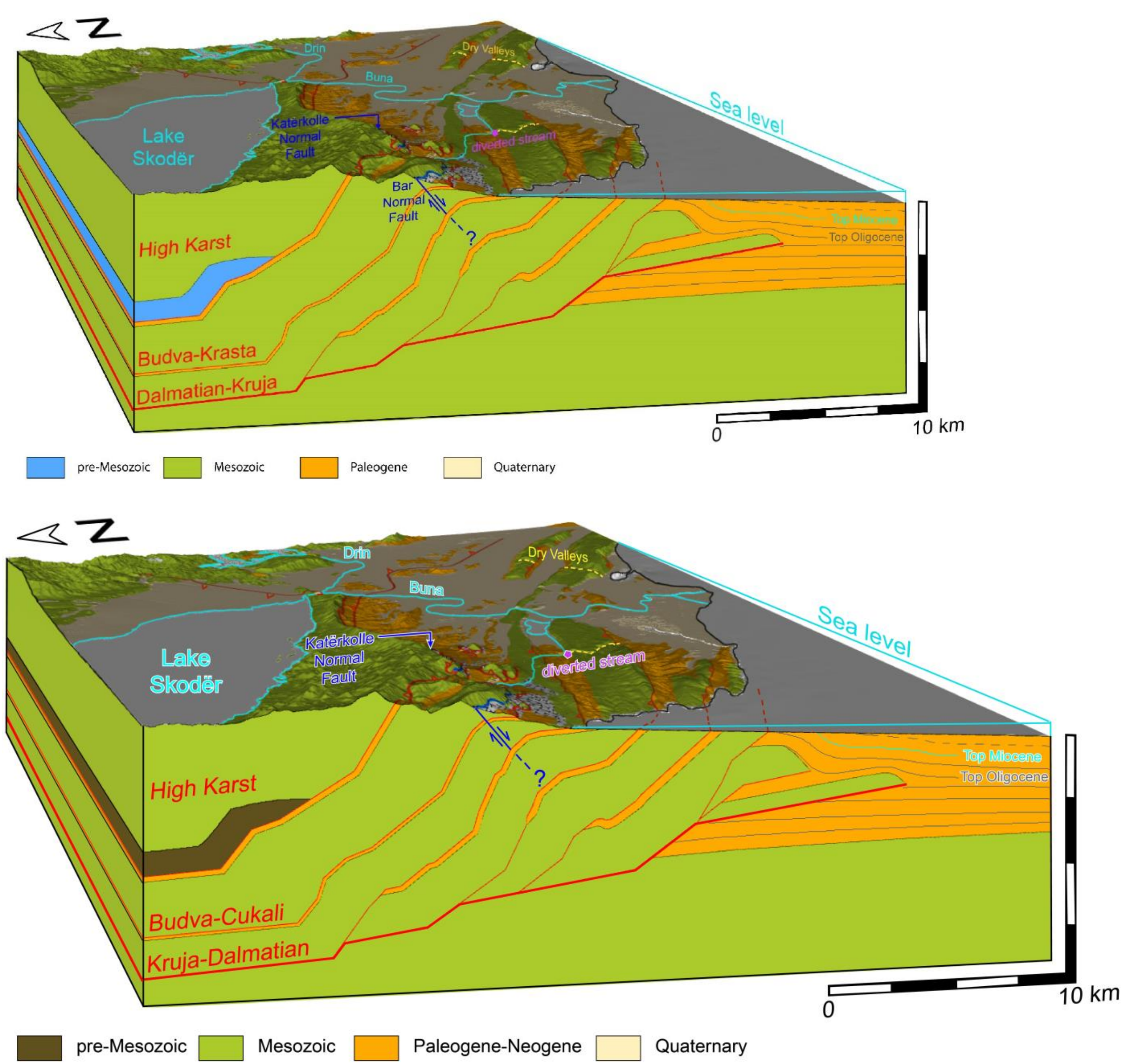

Figure 10: 3D block diagram of the tectono-morphological features of the Montenegro-Albanian coastal border region. Forward modelled structural cross section through the external Dalmatian nappe stack, modified after Schmitz et al. (2020). The spatial proximity of the extensional NFS and contractional dry valleys as well as a supposedly tectonically deviated stream (Biermanns et al. 2019, Schmitz et al. 2020) supports the conclusion of highly interactive tectonic regimes.